Title

Crystallographic and kinetic analyses of the FdsBG subcomplex of the cytosolic formate dehydrogenase FdsABG from Cupriavidus necator

Journal

Journal of Biological Chemistry, 295(19)

ISSN

0021-9258

Authors

Young, Tynan
Niks, Dimitri
Hakopian, Sheron
et al.

Publication Date

2020-05-01

DOI

10.1074/jbc.ra120.013264

Peer reviewed

Crystallographic and kinetic analyses of the FdsBG subcomplex of the cytosolic formate dehydrogenase FdsABG from *Cupriavidus necator*

Received for publication, March 2, 2020, and in revised form, March 30, 2020 Published, Papers in Press, April 5, 2020, DOI 10.1074/jbc.RA120.013264

Tynan Young, Dimitri Niks, Sheron Hakopian, Timothy K. Tam, Xuejun Yu, Russ Hille[1], and Gregor M. Blaha[2]

From the Department of Biochemistry, University of California, Riverside, California 92521

Edited by Ruma Banerjee

Formate oxidation to carbon dioxide is a key reaction in one-carbon compound metabolism, and its reverse reaction represents the first step in carbon assimilation in the acetogenic and methanogenic branches of many anaerobic organisms. The molybdenum-containing dehydrogenase FdsABG is a soluble NAD^+-dependent formate dehydrogenase and a member of the NADH dehydrogenase superfamily. Here, we present the first structure of the FdsBG subcomplex of the cytosolic FdsABG formate dehydrogenase from the hydrogen-oxidizing bacterium *Cupriavidus necator* H16 both with and without bound NADH. The structures revealed that the two iron-sulfur clusters, Fe_4S_4 in FdsB and Fe_2S_2 in FdsG, are closer to the FMN than they are in other NADH dehydrogenases. Rapid kinetic studies and EPR measurements of rapid freeze-quenched samples of the NADH reduction of FdsBG identified a neutral flavin semiquinone, $FMNH^•$, not previously observed to participate in NADH-mediated reduction of the FdsABG holoenzyme. We found that this semiquinone forms through the transfer of one electron from the fully reduced $FMNH^-$, initially formed via NADH-mediated reduction, to the Fe_2S_2 cluster. This Fe_2S_2 cluster is not part of the on-path chain of iron-sulfur clusters connecting the FMN of FdsB with the active-site molybdenum center of FdsA. According to the NADH-bound structure, the nicotinamide ring stacks onto the *re*-face of the FMN. However, NADH binding significantly reduced the electron density for the isoalloxazine ring of FMN and induced a conformational change in residues of the FMN-binding pocket that display peptide-bond flipping upon NAD^+ binding in proper NADH dehydrogenases.

The oxidation of formate to carbon dioxide is a key reaction in the metabolism of one-carbon compounds. In many anaerobic organisms, the reverse reaction represents the first step in carbon assimilation in both the acetogenic and methanogenic branches of the Wood–Ljungdahl pathway. The genome of *Cupriavidus necator* H16 (formerly known as *Ralstonia eutropha*) (1, 2) encodes four putative formate dehydrogenases, of which two are soluble NAD^+-dependent formate dehydrogenases. One of them is the molybdenum-containing dehydrogenase, FdsABG.

Formate dehydrogenase FdsABG forms a dimer of heterotrimers, $(\alpha\beta\gamma)_2$, with the 105-kDa FdsA subunit containing the active site molybdenum center and five iron-sulfur clusters, one Fe_2S_2 and four Fe_4S_4 clusters; the 55-kDa FdsB containing an Fe_4S_4 cluster, FMN, and a binding site for NADH/NAD^+; and finally, the 19-kDa FdsG subunit containing one Fe_2S_2 cluster. Although the physiological function of FdsABG is to oxidize formate to CO_2 by reducing NAD^+ to NADH (3–6), the enzyme has been shown to be fully capable of catalyzing the reverse reaction, the reduction of CO_2 to formate, using NADH as an electron source with steady-state kinetic parameters that conform to the required Haldane relationship (7).

Formate dehydrogenase FdsABG is a member of the NADH dehydrogenase superfamily, which is one of the most broadly distributed families of enzymes (5, 8–10). Members of this family typically couple electron transfer to generate a transmembrane proton or sodium gradient. The water solubility of FdsABG formate dehydrogenase greatly simplifies its biochemical study. Whereas the protein does not pump cations, it does contain redox-active centers that have been lost in other members of the superfamily over the course of evolution, including a bis(enedithiolate) molybdenum center that is the site of the fully reversible oxidation of formate to CO_2. As such, FdsABG is thought to represent, along with a separate hydrogenase and membrane-integral ion channel, an evolutionarily primitive, functional module of NADH dehydrogenases.

The FdsA, FdsB, and FdsG subunits have strong sequence homology to corresponding subunits in the cytosol-exposed arm of the membrane-integral and proton-pumping NADH dehydrogenase (3–6). FdsA is cognate to the Nqo3 subunit of the *Thermus thermophilus* NADH dehydrogenase (11, 12), despite the absence of the molybdenum center and of one of the Fe_4S_4 clusters (5). The close homology between FdsA and Nqo3 extends to the presence of a histidine ligand to one of the Fe_4S_4 clusters. The C terminus of FdsA, containing the molybdenum center, also has an ~60% sequence similarity to the structurally characterized FdhF formate dehydrogenase of *Escherichia coli*, with cysteine, Cys-378, equivalent to the molybdenum-coordinating selenocysteine, Sec-140, in FdhF (13). This C-terminal

This work was supported by discretionary funds of the University of California, Riverside (to G. M. B.) and by United States Department of Energy Grant DE-SC0010666 (to R. H.). The authors declare that they have no conflicts of interest with the contents of this article.

This article contains Table S1 and Figs. S1–S4.

[1] To whom correspondence may be addressed: Dept. of Biochemistry, University of California, Riverside, 900 University Ave., Boyce Hall 2404, Riverside, CA 92521. Tel.: 951-827-6354; E-mail: russ.hille@ucr.edu.

[2] To whom correspondence may be addressed: Dept. of Biochemistry, University of California, Riverside, 900 University Ave., Boyce Hall 5489, Riverside, CA 92521. Tel.: 951-827-3832; Fax: 951-827-4294; E-mail: gregor.blaha@ucr.edu.

domain is also present in Nqo3, although the molybdenum center has been lost over the course of evolution.

The FdsB subunit has ~45% sequence identity to the Nqo1 subunit of the *T. thermophilus* NADH dehydrogenase and, like Nqo1, contains an Fe_4S_4 cluster, FMN, and a binding site for NADH/NAD^+. As demonstrated here, it also possesses an N-terminal thioredoxin-like domain that lacks the typical iron-sulfur cluster and the disulfide bond of thioredoxin. The FdsG subunit has ~34% sequence identity to the Nqo2 subunit of the *T. thermophilus* NADH dehydrogenase and possesses an Fe_2S_2 cluster.

Under physiological conditions, electrons enter the FdsABG holoenzyme at the molybdenum center in the reductive half of the catalytic cycle and depart at the FMN in the oxidative half-reaction, with electron transfer between the two sites (thought to be separated by ~55 Å (9)) mediated by intervening iron-sulfur clusters.

Because FdsB- and FdsG-like domains are found in all members of the NADH dehydrogenase superfamily (12, 14), we have undertaken a study of the FdsBG subcomplex of *C. necator* formate dehydrogenase, with the aim of putting the oxidative half-reaction of the enzyme in a structural context. Here, we present the structure of FdsBG complex and characterize its kinetic properties.

Results

Previously, the FdsBG homologous, stand-alone complex of NADH dehydrogenase from *Paracoccus denitrificans* has been characterized and shown to be capable of NADH oxidation (15). We therefore set out to characterize the electron transfer reaction of the FdsBG complex from *C. necator*.

The recombinant expression of *C. necator* FdsABG holoenzyme in *E. coli* produces not only monomeric and dimeric holoenzyme, but also significant amounts of FdsBG complex (16). A similar observation was reported for the expression of *Rhodobacter capsulatus* FdsABG holoenzyme (17).

To streamline the purification of FdsBG complex, we redesigned the FdsABG holoenzyme expression system to produce only FdsBG complex with two different N-terminal tags on FdsG, His_6-linker-His_6 and Twin-Strep® tag. The resulting constructs produce FdsBG complexes that are substantially identical in their NADH/NAD^+ redox activity and their ability to crystallize. A detailed description of the two constructs and the purification of the overexpressed FdsBG complexes is provided under "Experimental procedures."

Characterization of the two iron-sulfur clusters of the FdsBG complex

We first examined the EPR signals attributable to the complex's two iron-sulfur centers. Upon extended incubation of FdsBG complex with dithionite, two signals are observed (Fig. 1*A*, *black trace*).

The first signal is seen at liquid nitrogen temperatures with *g*-values of $g_{1,2,3}$ = 2.000, 1.948, and 1.920 and line widths of 1.4, 1.7, and 1.6 mT,[3] respectively. These values are in good agreement with those described previously for the cluster designated as Fe/S_1 for the FdsABG holoenzyme (Fig. 1*B*, *blue dashed trace*) (6). This EPR signal is observed well into the 200 K regime.

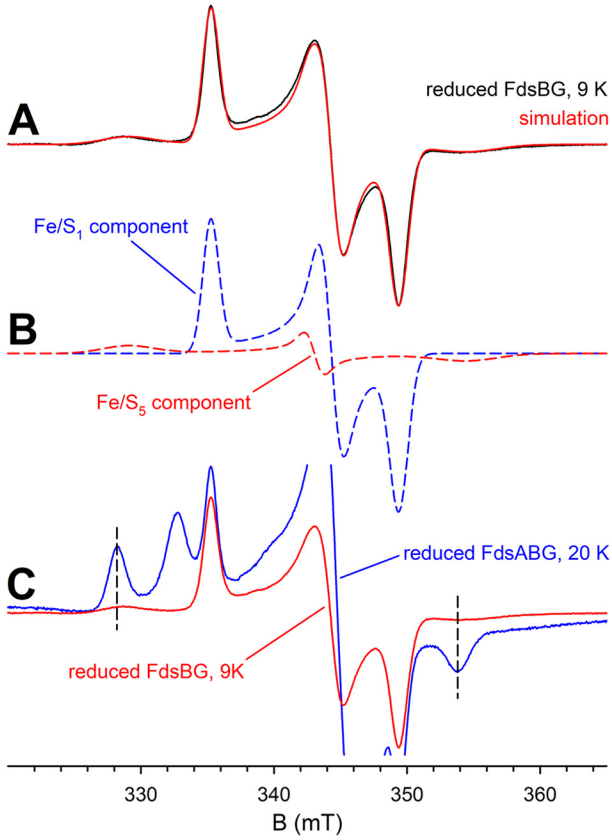

Figure 1. EPR spectra of the iron-sulfur clusters of the FdsBG complex. *A*, observed iron-sulfur EPR spectrum (*black trace*) and simulated composite spectrum (*red trace*) of the dithionite-reduced FdsBG complex, collected at 9 K with modulation amplitude of 8 gauss and microwave power of 2 microwatts. The sample was prepared by incubation of 125 μM of FdsBG complex in 100 mM KPO_4, pH 7.0, with 2 mM buffered sodium dithionite under anaerobic conditions for 1 h at room temperature prior to freezing. *B*, the individual component spectra resulting from the simulation of the composite spectrum in *A*: the spectrum corresponding to the previously assigned Fe/S_1 (*blue dashed trace* (6)) and an additional Fe/S_5 signal (*red dashed trace*) resolved only in the FdsBG complex. *C*, superposition and graphical alignment of the spectrum presented in *A* (*red trace*) with the spectrum of dithionite-reduced FdsABG collected at 20 K (*blue trace*, expanded to match the amplitude of the g_1 feature in the Fe/S_1 component of the FdsBG spectrum; reprinted with permission (6)). *Dashed lines* mark the location of g_1 and g_3 features of the Fe/S_3 component of the FdsABG holoenzyme spectrum.

The second signal is detected below 20 K with *g*-values of $g_{1,2,3}$ = 2.039, 1.955, and 1.891 and line widths of 4.5, 1.4, and 5.3 mT, respectively (Fig. 1*B*, *red dashed trace*). This cluster has not been described previously in the holoenzyme (6), and we now designate it as Fe/S_5.

In the homologous FdsBG complexes from NADH dehydrogenase (*Aquifex aeolicus* NuoEF or *T. thermophilus* Nqo1·2), only EPR signals of the Fe_2S_2 clusters are detectable above 77 K, whereas those for the Fe_4S_4 clusters appear only below 50 K (18). The *g*-values $g_{1,2,3}$ = 2.004, 1.945, and 1.917 for the N1a Fe_2S_2 cluster of the 24-kDa subunit of respiratory complex I from bovine mitochondria (the homolog to FdsG) are in excellent agreement with the Fe/S_1 signal. Accordingly, we assign the Fe/S_1 signal to the Fe_2S_2 cluster of FdsG (19). The signal

[3] The abbreviations used are: mT, milliteslas; RMSD, root mean square deviation; 2D, two-dimensional; OD, optical density; PDB, Protein Data Bank; ICP-OES, inductively coupled plasma-optical emission spectrometry; MWCO, molecular weight cuf-off.

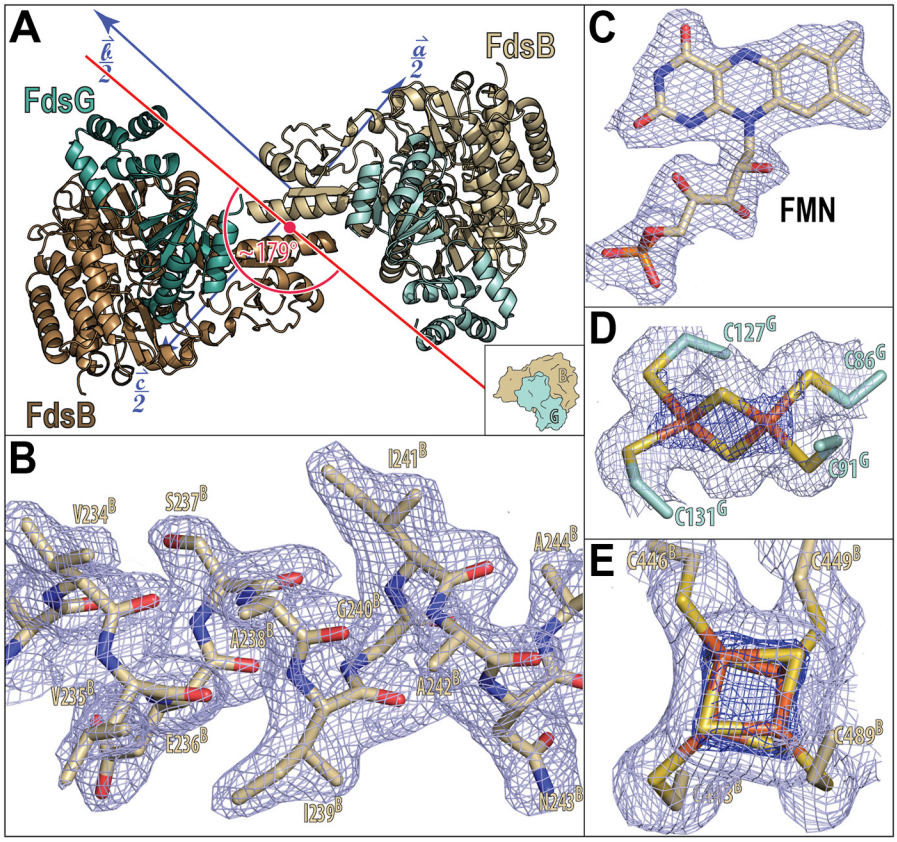

Figure 2. Arrangement of the two FdsBG complexes of the asymmetric unit and electron density map of representative regions. *A*, placement of the two FdsBG complexes of the asymmetric unit within the crystallographic unit cell. The view is down the ~179° rotation axis between the two FdsBG complexes of the asymmetric unit. Crystallographic axes are in *blue*, with the b-axis being the crystallographic 2-fold. The angle between the ~179° rotation axis and the crystallographic 2-fold (*i.e.* b-axis) is ~92°. *B–E*, the ($2F_o - F_c$)-electron difference map for different regions of the final model. *B*, the α-helical region between residues 234^B and 244^B (superscript B indicates that residues belong to FdsB) contoured at 1.0 σ and carve radius of 2.0 Å; *C*, the FMN bound to FdsB contoured at 1.0 σ and carve radius of 1.5 Å; *D*, the Fe_2S_2 cluster of FdsG contoured at 1.0 and 6 σ and carve radius of 2.5 Å; *E*, the Fe_4S_4 cluster of FdsB contoured at 1.0 and 6 σ and carve radius of 2.0 Å. The electron difference map contoured at 1.0 and 6.0 σ are shown as *light blue* and *blue meshes*, respectively.

assigned to the N3 Fe_4S_4 cluster in the NADH dehydrogenase system, with *g*-values of $g_{1,2,3} = 2.037, 1.945$, and 1.852, is also in good agreement with the Fe/S_5 signal of the FdsBG complex. Therefore, we assign the Fe/S_5 signal to the Fe_4S_4 cluster of FdsB.

We had initially assigned the Fe/S_1 signal to the His-coordinated Fe_4S_4 cluster contained in the FdsA subunit of the FdsABG holoenzyme (6), but that is clearly not the case as the signal is observed in the FdsBG complex. We note that the Fe/S_5 signal has very similar *g*-values to that reported for the previously observed Fe/S_3, although the Fe/S_5 line widths are considerably broader (see the g_1 and g_3 features of red and blue EPR spectra, centered around the *dashed lines* in Fig. 1*C*). However, the Fe/S_3 cluster has been shown to be magnetically coupled to the molybdenum center and must accordingly arise from the Fe_4S_4 cluster proximal to the molybdenum center in FdsA. Therefore, the Fe/S_5 signal must be a newly identified signal.

The assignment of the Fe/S_5 signal to the Fe_4S_4 cluster of the FdsB subunit is strengthened by the below described structure of the FdsBG complex and by our previously published structural model of the FdsABG holoenzyme (9). This model places the Fe_4S_4 cluster in the proximity of FdsA in the intact holoenzyme and in the electron path between the molybdenum and FMN. It is likely that the large line widths, in conjunction with the relatively low level of reduction and overlapping *g*-values with Fe/S_3, obscured its detection in the earlier work with the holoenzyme. It is also possible that the presence of additional, higher-potential clusters in the FdsA subunit prevents the reduction of the Fe/S_5 cluster in the holoenzyme.

Crystal structure of FdsBG complex: Overview

We further characterized the FdsBG complex by determining its structure by X-ray crystallography to 2.3 Å resolution (Fig. 2, *B–E*). The final phased electron density allowed us to build nearly all residues of the FdsBG heterodimer (for data and refinement statistics see Table S1). The heterodimer has dimensions of 82 × 64 × 62 Å, and the two heterodimers of the asymmetric unit are related by a noncrystallographic rotation of ~179° (Fig. 2*A*). The axis of rotation passes through the interface formed by the N-terminal thioredoxin-like domains of the two FdsB molecules of the asymmetric unit (residues 3^B–104^B, where the superscript B indicates that the residue belongs to FdsB). The unusual relationship of the two FdsBG complexes in the asymmetric unit notwithstanding, their structures are nearly identical, with an RMSD of 0.35 Å for

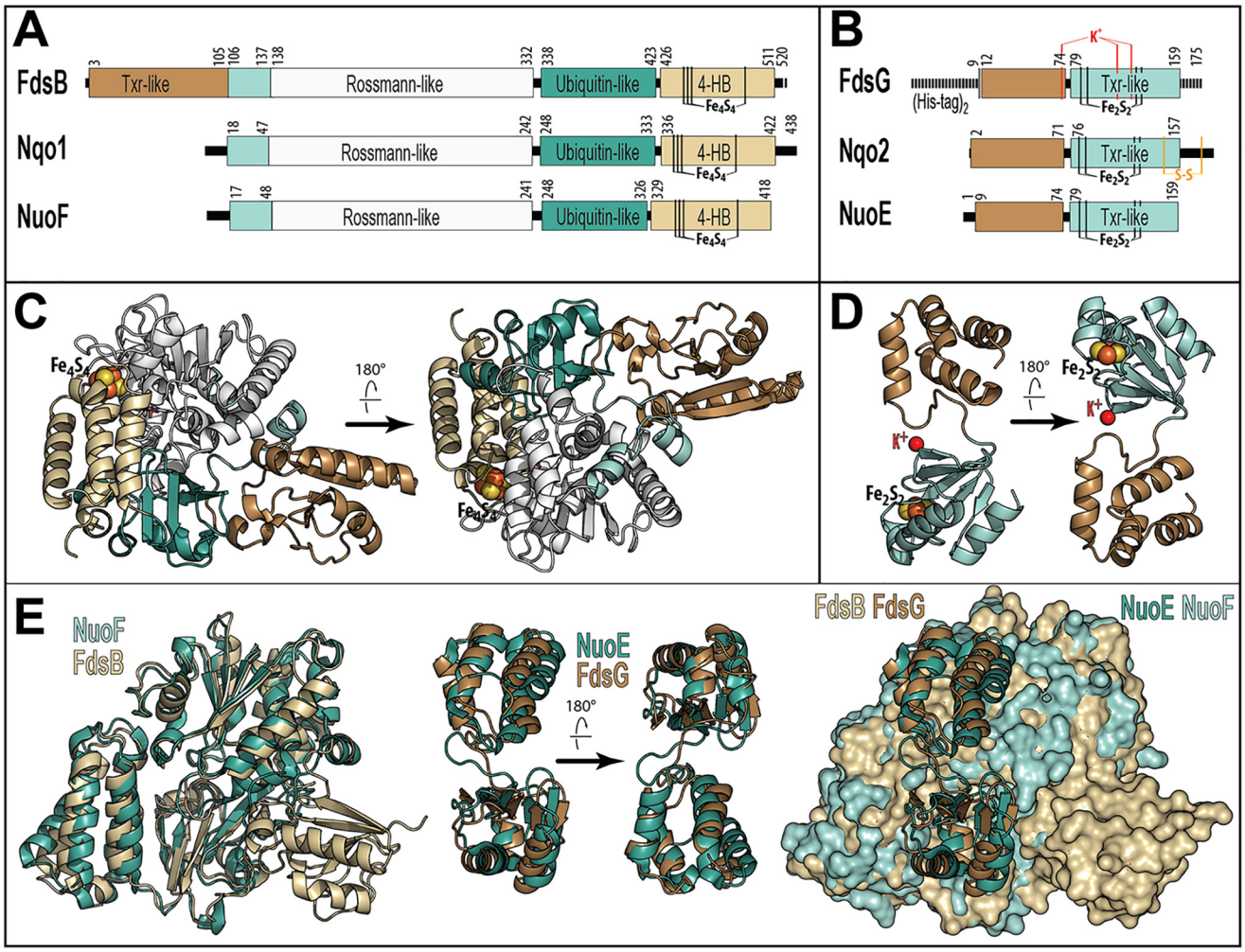

Figure 3. Domain structure of FdsB and FdsG and their sequence and structure alignment with NuoE and NuoF. *A*, primary structures of FdsB, Nqo1 from *T. thermophilus*, and NuoF from *A. aeolicus*. The domains are indicated as *boxed regions*. The FdsB-specific N-terminal thioredoxin-like domain (*Txr-like*), N-terminal region of Nqo1, Rossmann-like fold, ubiquitin-like domain, and four-helical bundle (*4-HB*) are shown in *brown*, *light green*, *white*, *green*, and *beige*. *B*, primary structures of FdsG, Nqo2, and NuoE. The N-terminal four-helical bundle and the thioredoxin-like domain (*Txr-like*) are shown in *brown* and *light green*. *C* and *D*, structures of FdsB and FdsG subunits with domains *color-coded* according to *A* and *B*. *E*, superposition of FdsB (*beige*) and NuoF (*light green*) subunits, of FdsG (*brown*) and NuoE (*green*) subunits, and of FdsBG (*beige* and *brown*) and NuoEF complexes (*light green* and *green*).

all the atoms of the 661 residues of the core of the 735-amino acid FdsBG complex. Each FdsBG complex contains two iron-sulfur clusters (one Fe_2S_2 and one Fe_4S_4 cluster), one FMN, and one K^+ ion. The final model also contains 498 water molecules.

For the detailed analysis of the structural differences between FdsBG complex and its homologous subcomplex from NADH dehydrogenase, we used the recently published, high-resolution structure from *A. aeolicus*, NuoEF complex (20). The NuoE subunit is homologous to the Nqo1 and FdsG subunits, and the NuoF subunit is homologous to the Nqo2 and FdsB subunits (Fig. 3, *A* and *B*).

Structure of the FdsB subunit of the FdsBG complex

Except for the N-terminal thioredoxin-like domain (residues 3^B–104^B), the FdsB subunit structure is highly similar to that of the NuoF subunit of the *A. aeolicus* NADH dehydrogenase (RMSD of 1.48 Å for 394 Cα atoms). Like NuoF, FdsB contains a Rossmann-like fold (residues 138^B–332^B, also classified as Complex I_51K domain (21)), a ubiquitin-like domain (residues 338^B–423^B), and a four-helical bundle (residues 426^B–511^B, NADH_4Fe-4S domain). The Rossmann-like fold contains the FMN-binding site, and the C-terminal four-helical bundle contains the Fe_4S_4 cluster (22) (Fig. 3*A*).

In the Rossmann-like domain, the main structural differences between the FdsB and NuoF subunits are in loops that are solvent-exposed. The only loop with a structural difference that is buried in the complex is positioned between the bound FMN and the Fe_2S_2 cluster of the FdsG subunit (183^B–190^B loop), thus enabling the Fe_2S_2 cluster to be ~0.2 Å closer to the FMN in the FdsBG complex than in the NuoEF complex (Fig. 4*A*).

The ubiquitin-like domain of FdsB is tilted toward the FMN bound in the Rossmann-like domain. This tilt toward the FMN propagates into the four-helical bundle domain, resulting in an ~0.2-Å distance closer between the FMN and the Fe_4S_4 cluster compared with that seen in the NuoEF complex (Fig. 4*B*). The Fe_4S_4 cluster is located in a hydrophobic environment close to the surface and is coordinated by Cys-443^B, Cys-446^B, Cys-449^B, and Cys-489^B (Fig. 2*E*).

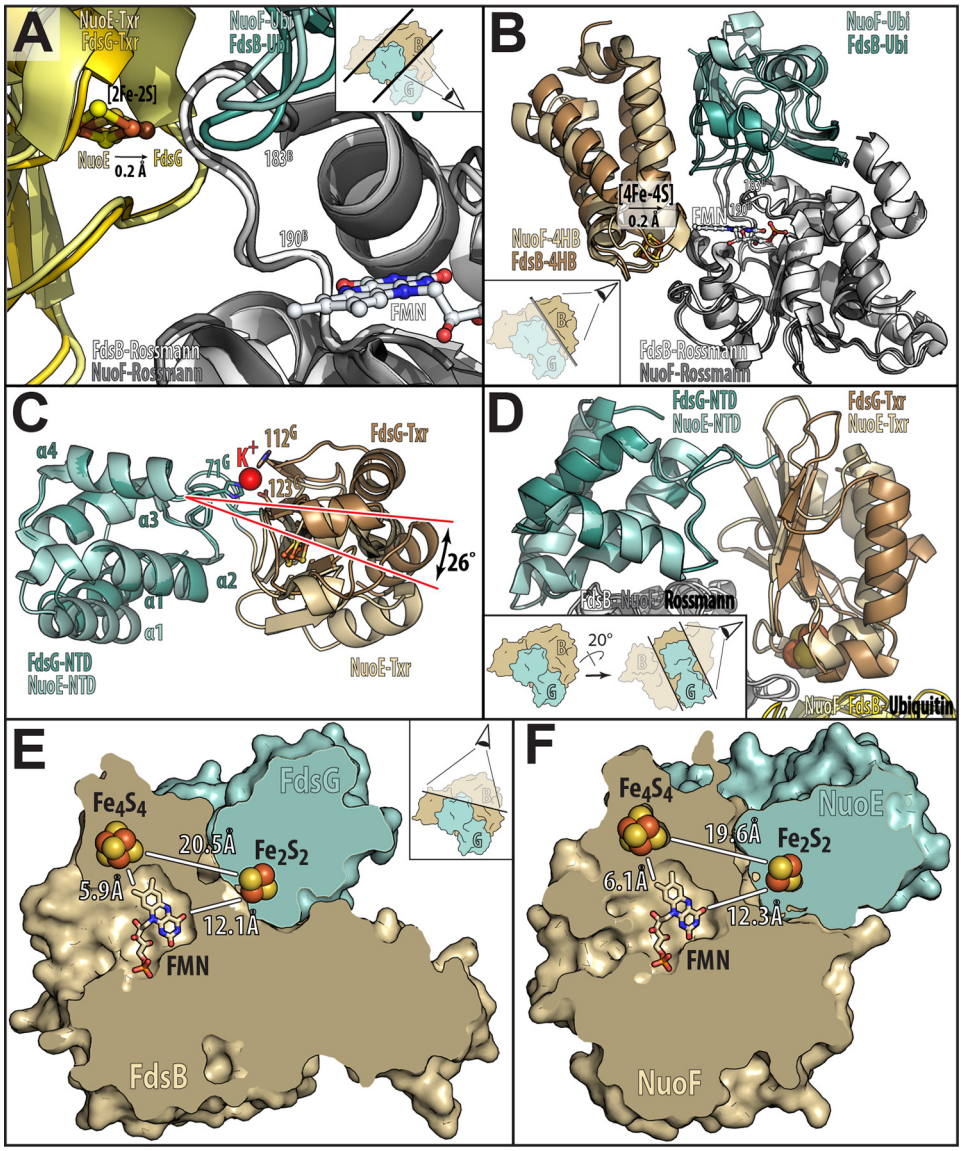

Figure 4. Structural comparison of the FdsBG and NuoEF complexes. *A* and *B*, effect of the structural difference in the 183^{B}–190^{B} loop of the Rossmann-like domain on the positioning of the Fe_2S_2 cluster (*A*), of the ubiquitin and four-helical bundle domains, and of the Fe_4S_4 cluster (*B*). The Rossmann-like, ubiquitin, and four-helical bundle domains of FdsB are displayed in *white*, *green*, and *brown*, and the C-terminal domain of FdsG is shown in *gold*. The corresponding domains of NuoF and NuoE are shown in *gray*, *light green*, *beige*, and *pale yellow*. *C*, difference in the C- and N-terminal domain arrangement of FdsG (*brown* and *green*) and NuoE (*beige* and *light green*). *D*, hinging of FdsG's C-terminal domain toward the Rossmann-like domain of FdsB compared with NuoE's C-terminal domain. *E* and *F*, overall arrangement of the Fe_2S_2 cluster, Fe_4S_4 cluster, and FMN in FdsBG (*E*) and NuoEF (*F*).

The N-terminal thioredoxin-like domain of FdsB is structurally similar to the C-terminal thioredoxin-like domain of FdsG (RMSD 1.97 Å for 71 Cα atoms of the core of the domain). However, unlike the domain in FdsG, that in FdsB has lost its capacity to bind an Fe_2S_2 cluster due to mutation of the corresponding cysteines to proline, alanine, serine, and phenylalanine, respectively (Pro-10^{B}, Ala-15^{B}, Ser-45^{B}, and Phe-49^{B}).

Structure of the FdsG subunit of the FdsBG complex

The structure of the FdsG subunit is also highly similar to the NuoE subunit of *T. thermophilus* NADH dehydrogenase. Like NuoE, FdsG consists of an N-terminal four-helical bundle (residues 29^{G}–74^{G}) and a C-terminal thioredoxin-like domain (residues 79^{G}–159^{G}). The domains are separated by a 4-amino-acid-long linker, around which the two domains are hinged by ~26° compared with NuoE. This domain arrangement is stabilized by a K^+ ion, which is held in place by residues from both domains (His-71^{G}, His-112^{G}, and Glu-123^{G}; Fig. 4*C*).

Although the N-terminal domains of FdsG and NuoE consist of a four-helical bundle, the first helix of FdsG packs in parallel to the second and third helix, whereas in NuoE it runs across the interface formed by these two helices (Fig. 4*C*). The C-terminal thioredoxin-like domain of FdsG is structurally similar to the N-terminal thioredoxin-like domain of FdsB but contains a spinach ferredoxin-like Fe_2S_2 cluster (22). The Fe_2S_2 cluster is located in a hydrophobic environment close to the surface and is coordinated by Cys-86^{G}, Cys-91^{G}, Cys-127^{G}, and Cys-131^{G} (Figs. 2*D* and 3*B*). Compared with Nqo2, FdsG's and NuoE's thioredoxin-like domains are truncated at their C termini and are missing a disulfide bond (Fig. 3*B*).

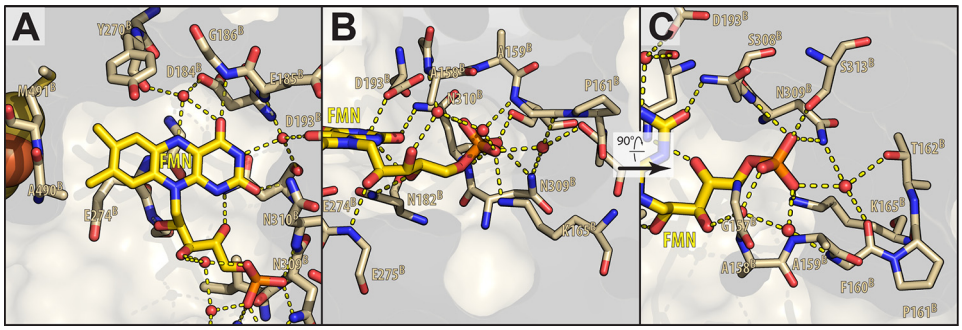

Figure 5. FMN-binding site. The binding site of the flavin ring (*A*) and of the ribityl-phosphate moiety (*B* and *C*) of FMN are displayed. The Fe_4S_4 cluster of FdsB is rendered in a *space-fill representation*, whereas FMN, residues of the binding site, and coordinating water molecules are rendered in a *ball-and-stick representation*. FMN, selected residues of FdsB, and water molecules are shown in *gold*, *beige*, and *red*, respectively.

The interface between FdsB and FdsG subunits in the FdsBG complex

Two helices of FdsG's four-helical bundle interact with the surface of the Rossmann-like domain of FdsB, similar to the interactions seen in the NuoEF interface (Fig. 4*D*). The C-terminal thioredoxin-like domain of FdsG binds to the same surfaces of the ubiquitin-like domain and Rossmann-like domain of FdsB as in the NuoEF complex. However, the different positioning of the ubiquitin and of the 183^B–190^B loop results in the Fe_2S_2 cluster of FdsG being an additional ~1.0 Å farther from the Fe_4S_4 cluster compared with the respective clusters in the NuoEF complex (Fig. 4, *E* and *F*).

With an edge-to-edge distance of nearly 21 Å, direct electron transfer between the Fe_2S_2 cluster and Fe_4S_4 cluster is unlikely to be kinetically significant. However, both clusters are within 12 Å of the isoalloxazine ring of FMN (Fig. 4*E*), which evidently mediates electron equilibration between the two iron-sulfur clusters. Whereas the Fe_4S_4 cluster of FdsB is clearly a part of the electron transport chain between the molybdenum center of FdsA and the FMN of FdsB, the Fe_2S_2 cluster of FdsG lies off-path and appears to function as a temporary repository for electrons in the course of electron egress out of the flavin (see "Discussion").

The FMN-binding site of the FdsB subunit

The FMN is bound by a network of interactions in an extended, solvent-accessible cavity that also accommodates NAD^+/NADH. The isoalloxazine ring of FMN is within 12 Å of each iron-sulfur cluster. The C8-methyl of the dimethylbenzene moiety of the flavin points toward the Fe_4S_4 cluster, and the N5-containing edge faces the Fe_2S_2 cluster, whereas the ribityl phosphate tail extends away from both iron-sulfur clusters (Fig. 4*E*).

The direct and water-mediated interactions between the FMN isoalloxazine ring and the ribityl phosphate tail with FdsB's Rossmann-like fold are conserved in the high-resolution structures of other members of the NADH oxidoreductase family (14, 20) (Fig. 5, *A*–*C*). (For a detailed description and the 2D representation of these interactions, see the supporting material and Fig. S1, respectively. For comparison, we also provide the 2D representation of the FMN interactions with the NADH dehydrogenase, NuoE, and the NAD^+-reducing hydrogenase, HoxF, as Figs. S2 and S3, respectively. These 2D representations of the interactions were prepared with LigPlot+ version 2.1 (23)).

Biochemical characterization of the bound FMN

In the absence of the FdsA subunit, which contains five iron-sulfur clusters and a molybdenum active site, the UV-visible spectrum of the isolated FdsBG complex is dominated by the spectral features of the FMN centered around 350 and 450 nm (Fig. 6*A*, *red spectrum*). In addition, a feature around 550 nm, attributed to the Fe_4S_4 and Fe_2S_2 clusters of the FdsBG complex, is significantly more pronounced due to the lack of interference of the additional iron-sulfur clusters present in the FdsABG holoenzyme (6). Removal of the FMN via TCA precipitation indicates that the FdsBG complex is ~50% saturated with FMN. This level of FMN saturation is comparable with the level of flavin saturation in the isolated FdsABG holoenzyme.[4] This incomplete FMN saturation in FdsBG suggests that we are visualizing in our crystal structures an average of at least two kinds of FdsBG, one with and one without FMN-bound, deflavo FdsBG.

A reductive titration with sodium dithionite results in a systematic bleaching of the absorbance throughout the UV-visible region (Fig. 6*A*, *blue spectrum*). At the end of the titration, the bleaching in the 550-nm region is incomplete, suggesting that the cluster principally responsible for the residual 550-nm absorption is the Fe_4S_4 cluster that is not fully reduced by dithionite. A plot of the fractional absorbance changes at 550 nm against that at 450 nm provides information about the relative order of reduction during titration. The changes at 550 and at 450 nm are dominated by the reduction of the iron-sulfur clusters and FMN, respectively. A concurrent reduction of iron-sulfur clusters and FMN will result in a diagonal in this plot. A deflection of the diagonal to the *top left* suggests an earlier reduction of iron-sulfur clusters, whereas deflection to the *bottom right* suggests an earlier reduction of FMN (24). The *inset* of Fig. 6*B* shows a deflection to the *top left* from the diagonal, indicating that at least one iron-sulfur cluster is reduced sooner than the FMN during titration with dithionite. This suggests that the FMN has a lower reduction potential relative to at least one of the iron-sulfur clusters.

[4] D. Niks and R. Hille, unpublished data.

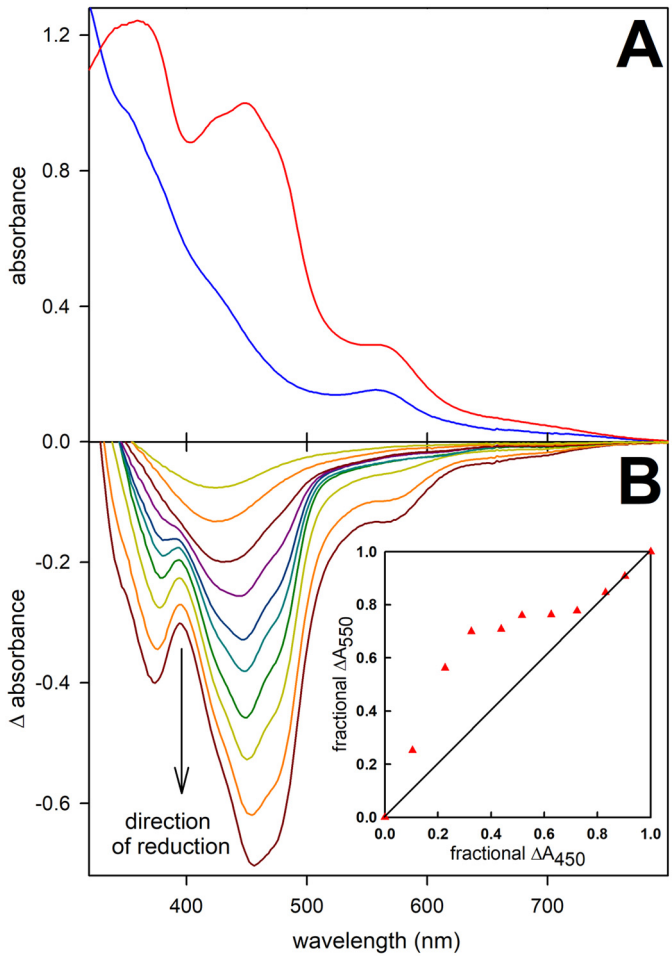

Figure 6. Reductive titration of FdsBG complex at pH 7.0. *A*, oxidized (*red*) and sodium dithionite-reduced (*blue*) spectra. *B*, change in absorbance as a function of reduction. The *inset* plots the relative absorbance change at 550 nm (*y* axis) against relative absorbance change at 450 nm (*x* axis) with the *diagonal* reflecting strict proportionality in the absorbance change between two wavelengths. The titration was performed at room temperature in 100 mM KPO_4, pH 7.0, under anaerobic conditions.

NADH binding to the FdsB subunit: Overview

To establish the NADH/NAD^+-binding site of the FdsBG complex, we solved the structure of FdsBG with bound NADH. To this end, preformed and stabilized FdsBG crystals were soaked with NADH at a final concentration of 10 mM in stabilization solution for 2 h, before flash freezing in liquid nitrogen. The crystal structure was solved to 2.0 Å by molecular replacement using the above described structure of the FdsBG complex as the initial search model. (See Table S1 for diffraction and refinement statistics.) Electron density for the adenosine diphosphate moiety of NADH is visible in the unbiased ($F_o - F_c$)-map of both FdsBG complexes of the asymmetric unit (Fig. 7*A*, *green mesh*). The overall protein structures of the FdsBG complexes are virtually identical in the presence and absence of NADH (RMSD 0.19 Å for the 1435 Cα atoms shared between the FdsBG complex on its own and NADH-bound structures).

As in the FdsBG structure by itself, the two NADH-bound FdsBG complexes of the asymmetric unit are highly similar (RMSD 0.34 Å for the 660 Cα atoms that the two FdsBG complexes share). However, the density for the isoalloxazine ring of FMN in each of two FdsBG complexes of the asymmetric unit is distinct. In one FdsBG complex, most of the FMN has significantly lower electron density than its terminal phosphate (Fig. 7*A*, *light blue versus blue meshes*). Due to our crystallization conditions, we speculate that the terminal phosphate is actually a sulfate bound to the fraction of FdsBG with no FMN bound.

FMN binding to FdsBG in the presence of NADH

Comparing the FMN-binding pocket of both FdsBG complexes in the asymmetric unit suggests that the peptidyl bond between Asp-184^B and Glu-185^B is pointing toward the O4 carbonyl oxygen of the isoalloxazine ring of FMN, in particular when less FMN is bound. The refinement of the FdsBG structure without FMN places the carbonyl oxygen of the Asp-184^B–Glu-185^B peptide bond so far into the FMN-binding pocket that it would encroach on the O4 of the isoalloxazine ring (Fig. 7*B*). This suggests that the change of the peptide bond position correlates with the loss of FMN.

NADH/NAD^+-binding site on FdsBG complex: The adenosine diphosphate moiety

More electron density is visible for the adenosine diphosphate of NADH than for the nicotinamide portion. This observation implies that the nicotinamide moiety of NADH contributes less to NADH affinity to FdsBG.

The β-phosphate of NADH is held in place by a salt bridge to FdsB and by two hydrogen bonds to the O2′ and O4′ hydroxyl groups of FMN's ribityl moiety (Fig. 7*D*). The adenosine base of NADH binds into a hydrophobic pocket. The O2′ hydroxyl and O3′ hydroxyl adenosine are within hydrogen bond distance of the carboxyl group of Glu-275^B. This places a negative charge adjacent to the O_2′, ensuring FdsBG's specificity for NAD^+/NADH over $NADP^+$/NADPH (25). (A more detailed description of the ADP-binding interactions with FdsB is provided in the supporting material.)

The specificity for the adenine base is brought about by the hydrogen bond from the side-chain hydroxyl group of Thr-168^B, which is specific to FdsB. In the NADH dehydrogenases and NAD^+-reducing hydrogenases, the threonine is replaced by either phenylalanine or leucine. This hydrogen bond interaction between the adenine base and threonine contributes to the more than 0.5-Å distant binding of the adenosine diphosphate relative to the FMN isoalloxazine ring compared with its binding in NuoF (Fig. 7*C*).

Binding of the nicotinamide ring of NADH relative to the isoalloxazine ring of FMN

Although only weak electron density is evident for the nicotinamide ring of NADH in the structure of both FdsBG complexes of the asymmetric unit, the direction of the two phosphates visible in the electron density suggests that the nicotinamide is projected toward the solvent-exposed *re*-face of the isoalloxazine ring of FMN. We therefore suggest that the nicotinamide moiety of NAD^+/NADH stacks onto the *re*-face of the isoalloxazine ring during the actual electron transfer step, similar to what is observed in the NuoEF complex with bound NAD^+ and NADH (Fig. 7*C*) (20). However, the more distant binding of the adenosine relative to the isoalloxazine ring suggests that the nicotinamide ring will also be displaced over the

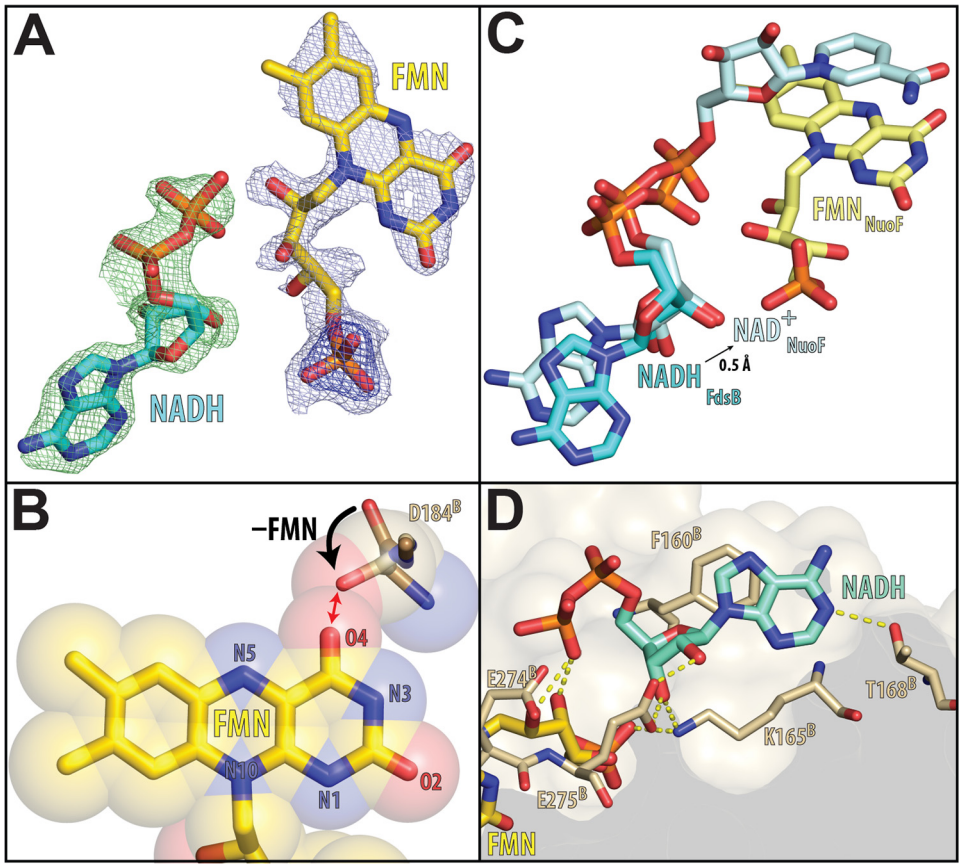

Figure 7. NADH binding site. *A*, the unbiased ($F_o - F_c$)- and ($2F_o - F_c$)-electron difference maps for FdsBG crystals soaked with NADH. The final models for FMN and the adenosine diphosphate of NADH are displayed in *ball-and-stick* (*gold* and *cyan*). The ($F_o - F_c$)-electron difference map contoured at 3.0 σ with a carve radius of 1.8 Å and the ($2F_o - F_c$)-electron difference map contoured at 1.0 and 3.0 σ with a carve radius of 1.8 Å are shown in *pale green*, *light blue*, and *blue meshes*, respectively. *B*, steric overlap between the Asp-184^B–Glu-185^B peptide bond with FMN in crystals of FdsBG complex soaked with NADH. The position of the Asp-184^B–Glu-185^B peptide bond shown was determined for FdsBG complex without FMN bound. *C*, comparison of the NADH/NAD$^+$ positions relative to the FMN of the NADH-bound FdsBG and the NAD$^+$-bound NuoEF complex. Shown are the FMN and NAD$^+$ from the NuoEF complex (*pale cyan* and *light yellow*; PDB entry 6HLI) and the NADH of the FdsBG complex (*cyan*). *D*, binding site of adenosine diphosphate of NADH. Displayed are FMN, NADH, and the adenosine-binding site on FdsB in *gold*, *blue*, and *beige*. Residues Val-295^B–Ala-297^B and Lys-292^B are omitted from this view for clarity.

isoalloxazine ring during the electron transfer reaction as compared with that in NuoF.

Rapid-reaction kinetics of the electron transfer reaction of the FdsBG complex

Due to the high velocity of the electron transfer reaction, we performed the rapid-reaction kinetics of FdsBG reduction by NADH at 5 °C. Although this is the reverse of the physiological reaction for the formate dehydrogenase, it is the physiological direction seen in NADH dehydrogenase and most other members of this enzyme family. As illustrated by a typical kinetic trace in the *inset* of Fig. 8, the reaction is biphasic. The fast phase of the reaction is complete within 120 ms. A plot of the observed rate constant for the fast phase as a function of NADH concentration is hyperbolic (Fig. 8), yielding a limiting k_{red} of 680 s^{-1} at high concentration of NADH and a K_d^{NADH} of 190 μM. Assuming a doubling of the rate constant for every 10 °C increase in temperature, this corresponds to a limiting k_{red} of 3850 s^{-1} at 30 °C, a rate that is more than 6-fold faster than the limiting rate of reduction of FdsABG holoenzyme at high concentration of formate, some 20-fold faster than the k_{cat} of the FdsABG holoenzyme for formate oxidation (6) and 350-fold faster than the k_{cat} for CO_2 reduction (7).

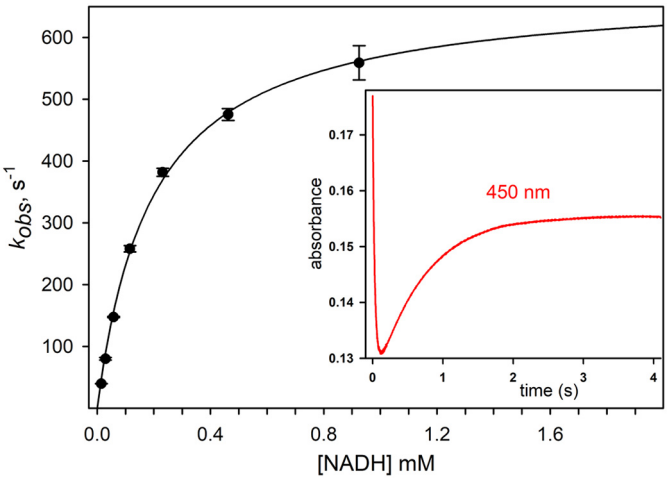

Figure 8. Single-wavelength pre-steady-state kinetics for the reduction of FdsBG with NADH. Shown is a plot of k_{obs} (*black circles*) *versus* NADH concentrations. Hyperbolic fits (*solid line*) yielded a k_{red} of 680 s^{-1} and K_d of 0.19 mM. Each *point* is the average of 3–5 measurements, and the *error bars* are the S.D. of these measurements. The *inset* shows a typical trace for the reaction of 9 μM FdsBG complex with 14 μM NADH monitored at 450 nm. All reactions were performed at 5 °C in 100 mM KPO_4, pH 7.0, under anaerobic conditions.

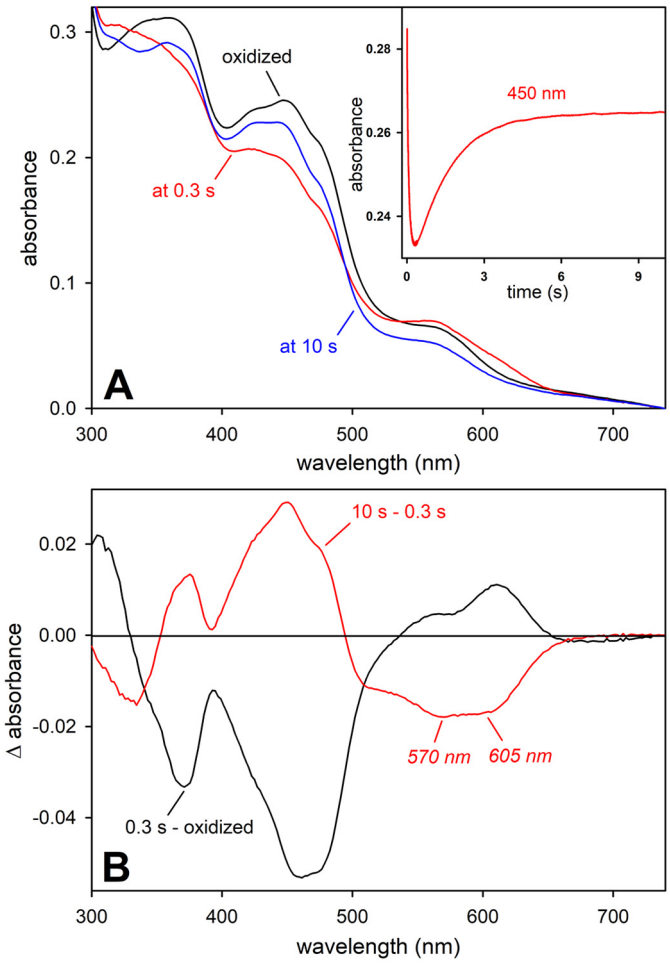

Figure 9. Rapid-reaction kinetics for the reaction of FdsBG with NADH. *A*, selected traces for the reaction of 10 μM FdsBG complex with 5 μM NADH at 5 °C in 100 mM KPO_4, pH 7.0, performed under anaerobic conditions and monitored with a photodiode detector. The oxidized spectrum was obtained by diluting FdsBG complex with buffer in the stopped-flow instrument. The *inset* shows a time course extracted at 450 nm. *B*, difference spectra from the data presented in *A*.

Formation of a neutral FMNH• semiquinone intermediate in the course of the reaction of FdsBG complex with NADH

At the completion of the fast phase of the reaction of 10 μM FdsBG complex with 5 μM NADH, the transiently observed UV-visible spectrum exhibits absorption in the 500–550-nm region consistent with the appearance of a neutral flavin semiquinone (FMNH•) (Fig. 9*A*, *red 0.3-s spectrum*). This species, not seen with the FdsABG holoenzyme, is the result of transfer of a single electron from the fully reduced flavin hydroquinone formed in the initial reaction with NADH to one or the other of the iron-sulfur clusters, leaving an FMNH• semiquinone behind; as described further below, this iron-sulfur cluster is the Fe_2S_2 cluster of FdsG giving rise to the Fe/S_1 EPR signal (see also Scheme 1).

On a longer timescale, the system disproportionates to some degree in a second-order process (Fig. 9*A*, *blue 10-s spectrum*), with an electron passing between two equivalents of $FdsBG_{2e-}$ to give one equivalent each of $FdsBG_{1e-}$ and $FdsBG_{3e-}$. The $FdsBG_{1e-}$ will have its Fe_2S_2 cluster (Fe/S_1) reduced and its FMN oxidized, and $FdsBG_{3e-}$ will have both Fe/S_1 and the

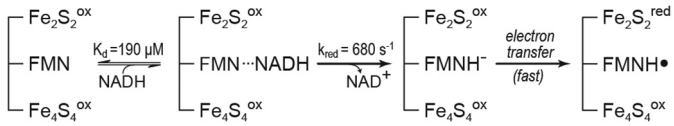

Scheme 1. Proposed electron transfer in FdsBG upon NADH reduction.

FMN reduced. The reaction shown in Fig. 9*A* was carried out with substoichiometric NADH so that the $FdsBG_{1e-}$ formed will not be further reduced by reaction with a second equivalent of NADH. The *inset* of Fig. 9*A* displays the kinetic time course obtained at 450 nm (extracted from the full data set collected with a photodiode array detector), showing both the fast reduction and the much slower disproportionation reactions.

We note that FdsBG may also involve a comproportionation reaction of $FdsBG_{2e-}$ with the deflavo form of FdsBG complex (which accounts for ~50% of the total protein as described above). Whereas the deflavo form cannot be reduced by NADH due to the absence of the FMN, it can accept electrons from the fully constituted and reduced $FdsBG_{2e-}$, resulting in one equivalent of $FdsBG_{1e-}$ with an oxidized FMN and reduced Fe/S_1 and a deflavo $FdsBG_{1e-}$ containing only a reduced Fe/S_1.

As the two processes are expected to proceed on at least approximately the same time scale, at the end of the redox reaction, there will be an excess of enzyme containing more oxidized than reduced flavin. An analysis of the slow phase of the reaction (described under "Experimental procedures") yields a second-order rate constant for this redox reaction on the order of 10^5 M^{-1} s^{-1}. It is noteworthy that, particularly at higher NADH concentrations, that the amplitude of the dis-/comproportionation phase decreases as the oxidized FMN thus generated becomes re-reduced by reaction with a second equivalent of NADH (data not shown).

Characterization of the neutral semiquinone intermediate, FMNH•

The spectral signature of the FMNH•, which has not been characterized previously in the FdsABG holoenzyme, can be best observed in the difference spectra presented in Fig. 9*B*. At the completion of the fast phase described by the absorbance difference between the spectrum of the fully oxidized enzyme subtracted from the spectrum collected at 0.3 s after the initial reaction of FdsBG with NADH (*black difference spectrum*). A positive feature consistent with the formation of the FMNH• is observed in the 500–650-nm region, although attenuated by the decrease in the absorbance due to the concurrent reduction of the iron-sulfur clusters. The complex negative feature in the 300–500-nm region is dominated by the loss of absorbance associated with iron-sulfur reduction as well.

The disappearance of the FMNH• is also evident in the end of the second, slow phase of the reaction (and is even more distinct, being unaffected by any further reduction of the iron-sulfur clusters). In the difference spectrum obtained by subtracting the spectrum collected at 0.3 s from that at 10 s after initial reaction with NADH (*red difference spectrum*), the 500–650-nm region is defined by two broad peaks centered at 570 and 605 nm, characteristic of the presence of FMNH• (26). The features are negative as they reflect the disappearance of the FMNH•.

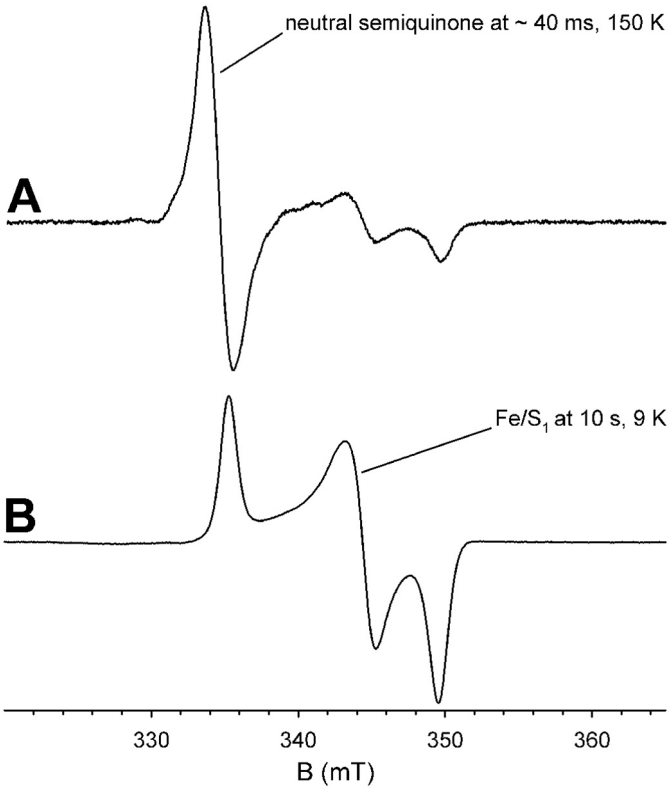

Figure 10. EPR of the neutral flavin semiquinone, FMNH• of FdsBG. *A*, sample was prepared by rapid freeze-quench of a reaction of 40 μM enzyme with 0.8 mM NADH at 0 °C (quenching time ~40 ms). The EPR spectrum was collected at 150 K with modulation amplitude of 8 gauss and microwave power of 0.4 milliwatts. *B*, sample was prepared by mixing 160 μM FdsBG with 60 μM NADH at room temperature for 10 s prior to freezing. The EPR spectrum was collected at 9 K with modulation amplitude of 8 gauss and microwave power of 2 microwatts. All samples were prepared in 100 mM KPO_4, pH 7.0, under anaerobic conditions.

Further evidence for the presence of a neutral semiquinone intermediate FMNH• comes from EPR measurements. To capture the transiently formed FMNH•, the enzyme was reacted with NADH at 0 °C and rapid freeze-quenched with a quenching time of ~40 ms. Fig. 10*A* shows the resulting spectrum collected at 150 K.

The 150 K EPR spectrum includes contributions from both FMNH• and Fe/S_1, demonstrating that it is the Fe_2S_2 cluster of FdsG that has been reduced. Graphical subtraction of the Fe/S_1 signal from the measured EPR spectrum yields an isotropic EPR signal with a $g_{iso} = 2.003$ and a line width of ~1.9 mT, which is indicative of a neutral rather than an anionic semiquinone (27, 28). Integration of both the scaled Fe/S_1 spectrum and the FMNH• spectrum from the graphical subtraction yielded a spin density ratio Fe/S_1:FMNH• of 1:0.7, consistent with the formation of FMNH• and reduction of only a single iron-sulfur cluster at the end of the fast phase of the NADH reduction of the FdsBG complex. No additional iron-sulfur signal was seen at 9 K either (data not shown).

To ascertain whether reduction of the Fe/S_5 cluster occurred during the slow, second phase, an additional sample was prepared by incubating FdsBG complex with an excess of NADH for 10 s under anaerobic conditions. The resulting spectrum recorded at 9 K is shown in Fig. 10*B*. The spectrum illustrates that only the spectrum corresponding to a single iron-sulfur cluster, Fe/S_1, is present at the end point of the second, slow phase of the NADH reduction reaction. Taken together, these results indicate that the fully reduced $FMNH_2$ initially formed on reaction with NADH breaks down by electron transfer of a single electron to the Fe_2S_2 cluster (Fe/S_1), with the second electron remaining as FMNH•; the Fe_4S_4 cluster (Fe/S_5) remains oxidized (see Scheme 1).

Discussion

The genome of *C. necator* H16 (1, 2) encodes four putative formate dehydrogenases, of which two are soluble NAD^+-dependent formate dehydrogenases. One of them is a molybdenum-containing dehydrogenase (FdsABG), and the other is a tungsten-containing dehydrogenase (FdwAB) (29). Whereas the FdsB of the molybdenum-containing dehydrogenase has an additional N-terminal thioredoxin-like domain, the FdsB homolog of the tungsten-containing dehydrogenase is N-terminally fused to its FdsG homolog to form FdwB. Two other NADH oxidoreductases with homology to FdsABG and FdwAB are also present in *C. necator*—NADH dehydrogenase and NAD^+-reducing hydrogenase.

Functional relevance of the N-terminal thioredoxin-like domain of FdsB

The N-terminal thioredoxin-like domain of FdsB has structural similarity to the thioredoxin-like Fe_2S_2 ferredoxin domain from *A. aeolicus* (21) (RMSD of 1.67 Å of 89 Cα atoms between both domains). The *A. aeolicus* domain is known to dimerize. The largest contact interface between two FdsBG complexes within the asymmetric unit is formed between the two thioredoxin-like domains. This suggests that the thioredoxin-like domain of FdsB contributes to the dimerization of the FdsABG holoenzyme.

We suggest, however, because of (*a*) the relative small size of ~560 $Å^2$ of the buried area, (*b*) the presence of only a few interactions across the interface (Fig. S4, *A–D*), (*c*) the low conservation of the residues at the dimer interface (Fig. S4, *E* and *F*), and (*d*) the absence of a dimeric form in solution during purification (data not shown), that the dimer formation in the asymmetric unit is merely due to crystal packing (30, 31) and does not participate in the dimerization of the FdsABG holoenzyme.

Although the N-terminal thioredoxin-like domain of FdsB is absent in other members of the NADH dehydrogenase family, it may nevertheless contribute to the stability of FdsB within the FdsABG holoenzyme. Protein stability is apparently a concern for some members of the family, as FdwB and HoxF have their FdsG and FdsB homologs fused. The linker between the FdsB-FdsG homologs overlaps structurally with the N-terminal thioredoxin-like domain of FdsB. The absence of the Fe_2S_2 cluster in the FdsG homologous region of FdwB and HoxF might destabilize this region to such an extent that its stability is only maintained by the fusion to their FdsB homologous regions.

Finally, we cannot exclude the possibility that the N-terminal thioredoxin-like domain provides an interface for an unknown partner. This partner may either participate in the redox reaction or provide a connection to the cell's metabolic status, such as ACP does in the case of NADH dehydrogenase (32, 33).

Characterization of FdsBG complex

Electron transfer mechanism in FdsBG

In the FdsABG formate dehydrogenase of *C. necator*, the reducing equivalents from the oxidation of formate pass through a chain of iron-sulfur clusters from the molybdenum center in FdsA to the FMN in FdsB, which ultimately reduces NAD^+. The FdsBG subcomplex can perform this ultimate step of reducing NAD^+, as can the corresponding subcomplexes from both NADH dehydrogenase (15, 20, 34) and NAD^+-reducing hydrogenase (35).

In our FdsBG structure, the Fe_4S_4 cluster of FdsB is in close proximity to the C8-methyl of FMN and to highly conserved surface residues that are implicated in the interaction of FdsB with FdsA (*i.e.* Glu-441^B–Ser-487^B, Ile-451^B–Gly-452^B, and Lys-292^B–Leu-298^B). This is consistent with the Fe_4S_4 cluster being on-path between the FMN and the molybdenum center of the FdsABG holoenzyme. The Fe_2S_2 cluster of FdsG, on the other hand, is farther away from residues implicated in FdsA binding and is also too far from the Fe_4S_4 cluster to directly take part in electron transfer from the molybdenum center to the bound FMN.

Nevertheless, it is clear from the evidence presented here that the initial electron transfer event out of the FMN upon reduction by NADH is to the off-path Fe_2S_2 cluster (having the higher reduction potential) rather than to the on-path Fe_4S_4 cluster (with much lower potential), as shown in Scheme 1. This process has not been observed previously in the reduction of either the FdsABG holoenzyme or the NADH dehydrogenase by NADH. It is thought that a similar off-path electron transfer minimizes the formation of reactive oxygen species in NADH dehydrogenase by minimizing the accumulation of neutral flavin semiquinone, $FMNH^\bullet$ (22, 36). In the case of FdsBG, the on-path electron transfer from the fully reduced flavin hydroquinone to the Fe_4S_4 cluster, to the extent that it occurs, leaves a neutral flavin semiquinone, $FMNH^\bullet$. This semiquinone would then rapidly transfer the second electron to the Fe_2S_2 cluster, thereby minimizing accumulation of the neutral semiquinone in the NADH dehydrogenase.

Implications for electron transfer in other members of the NADH dehydrogenase superfamily

Detailed structural analysis of the reduced and oxidized NuoEF complex from *A. aeolicus* revealed that the peptide bond between Glu-95^F and Ser-96^F of NuoF undergoes a reversible flip, depending on the oxidation state of the protein (20). In the oxidized state, the carbonyl group of Glu-95^F points to the FMN, whereas in the reduced state, it points to the Fe_2S_2 cluster (Fig. 11*D*).

The equivalent peptide bond in the FdsBG complex (Glu-185^B–Gly-186^B) adopts the same orientation in either state, oxidized or reduced (*i.e.* FdsBG as isolated and in the presence of NADH, respectively; Fig. 11*C*). However, in a subpopulation of the reduced FdsBG complex, the peptide bond prior to the oxidation state–sensitive peptide bond (Asp-184^B–Glu-185^B) is pointing toward the isoalloxazine ring of FMN, even encroaching on its O4 carbonyl oxygen. We have attributed this encroachment to the low FMN occupancy of the NADH-reduced FdsBG.

We note that this region of the protein is not particularly well-conserved between NuoF and FdsB (94^F-D**ES**EP-98^F *versus* 184^B-D**EG**DS-188^B; the residues of the peptide that reorients dependent on the oxidation state in NuoEF are shown in boldface type; see also Fig. 11*B*). The equivalent region in HoxF (232^F-D**EG**EP-236^F) appears to be flexible as well. As HoxF is devoid of an Fe_2S_2 cluster (one cysteine coordinating the Fe_2S_2 cluster is an alanine, and another cysteine is a serine), it is more likely that the absence of FMN in the reduced state of the Hox complex allows this peptide region to undergo the conformational change (14). These observations highlight the inherent flexibility of this region but also suggest that the oxidation state–dependent flipping of the peptide bond may be unique to the proper NADH dehydrogenase and not shared across the family.

Conclusion

In the present work, we have determined the X-ray crystal structure of the FdsBG portion of the FdsABG holoenzyme and characterized its interaction with NADH. The flexible region between the FMN and the Fe_2S_2 cluster in NADH dehydrogenase has recently been reported to undergo a conformational change dependent on the oxidation state in proper NADH dehydrogenases; however, an oxidation state–dependent conformational change is not seen here with the formate dehydrogenase.

In addition, we see for the first time the formation of a neutral semiquinone, $FMNH^\bullet$, in the course of reduction by NADH as a result of an electron transfer from the fully reduced flavin hydroquinone to the Fe_2S_2 cluster. The hydroquinone is generated upon reaction with NADH. The electron transfer to the Fe_2S_2 cluster is off-path with respect to the electron transfer pathway to the molybdenum center, where the enzyme reduces CO_2 to formate in the FdsABG holoenzyme. The electron transfer to the Fe_2S_2 cluster occurs over a distance of some 12 Å, with a rate constant that must exceed that for the NADH concentration–dependent rate of FMN reduction. The rate of FMN reduction is the rate-limiting step for electron transfer and occurs with a rate of at least 680 s^{-1} at 5 °C. This electron transfer process to the Fe_2S_2 cluster, observed here for the first time, has previously been proposed to play a role in limiting reactive oxygen species generation in the case of NADH dehydrogenase.

Experimental procedures

Cloning, protein expression, and protein purification of FdsABG holoenzyme and FdsBG subcomplex

The *fdsGBACD* operon with a His_6-linker-His_6 tag fused to the N terminus of the FdsG subunit was cloned into a pTrcHisB vector to construct the pTrc12HLB-FdsGBACD plasmid as described previously (16).

For protein expression, the plasmid was transformed into *E. coli* DH5α cells. By varying expression conditions, protein synthesis was optimized for production of FdsBG complex at the expense of FdsABG holoenzyme. For the optimized procedure, a 50-ml starter culture of Luria broth medium with 100 μg/ml ampicillin was inoculated from a glycerol stock of the DH5α transformed cells and grown overnight at 37 °C. The overnight culture was used to inoculate three 6-liter Erlenmeyer flasks, each containing 2 liters of TB medium supple-

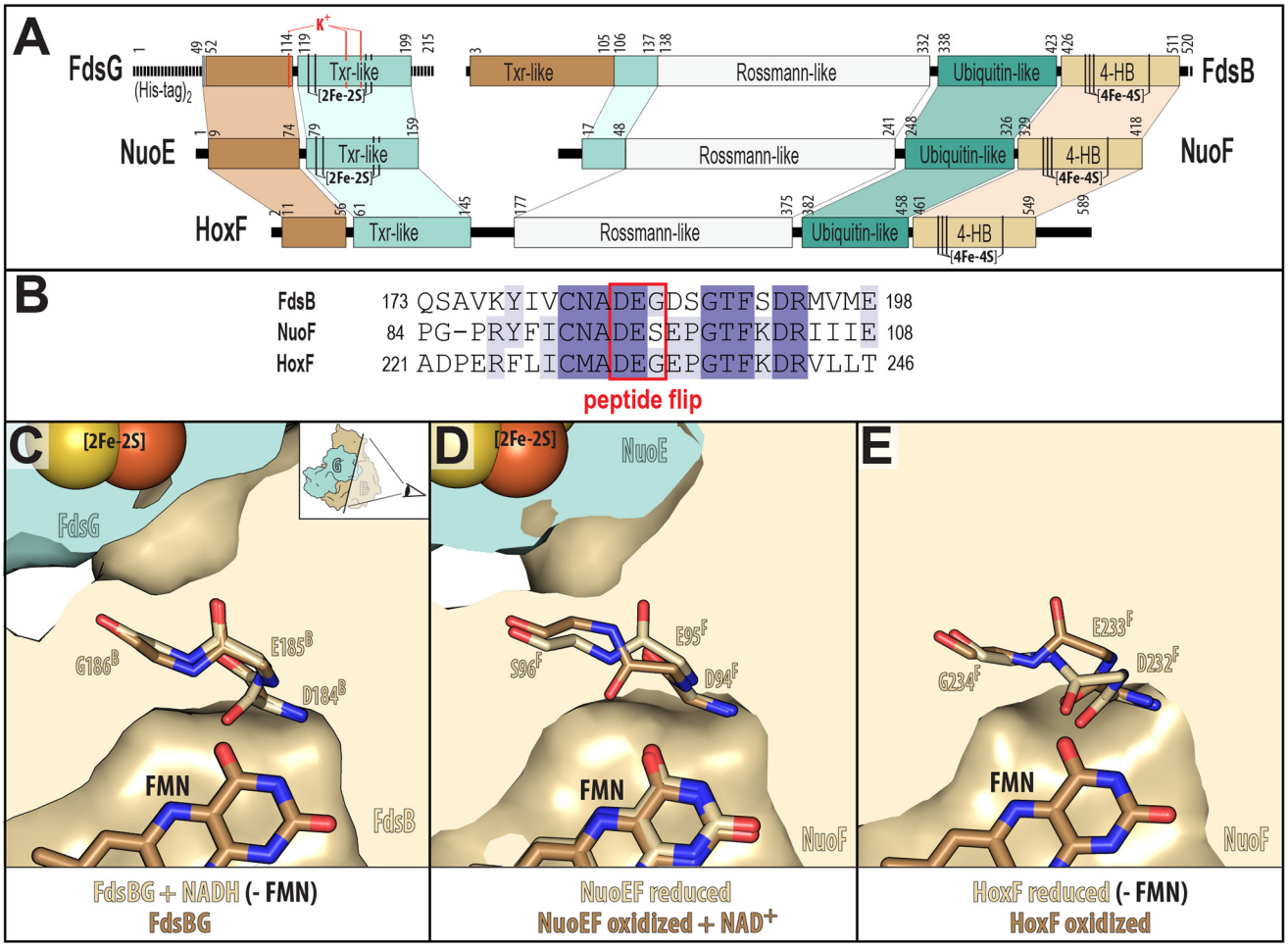

Figure 11. Sequence and structure comparisons of FdsBG, NuoEF, and HoxF. *A*, comparison of the domain structure of FdsB, FdsG, NuoE, NuoF, and HoxF. *B*, sequence alignment of the FdsB, NuoF, and HoxF regions for which an oxidation state–dependent peptide flip has been reported in NuoEF. *C*, structure comparison of FdsBG in the presence and absence of NADH. *D*, structure of NuoEF by itself (PDB entry 6HL2) and in oxidized form with bound NAD^+ (PDB entry 6HL3). *E*, structure of HoxFUHY in reduced form (PDB entry 5XFA) and oxidized form (PDB entry 5XF9). Shown is the main chain in the region of interest for each protein. The "reduced" and "oxidized" form of each protein is shown in *beige* and *brown*, respectively. Also indicated (*−FMN*) is the absence of FMN in the NADH-bound FdsBG and H_2-reduced HoxFUHY structures.

mented with 100 μg/ml ampicillin and grown at 30 °C and 200 rpm to an OD_{600} ~0.4, at which time they were induced with 0.25–0.5 mM isopropyl 1-thio-β-D-galactopyranoside. The induced cells were grown for an additional 44–48 h until OD_{600} reached ~10. Harvested cells were frozen in liquid nitrogen and stored at −80 °C until further use.

The plasmid pTrc12HLB-FdsGBACD was modified by removing the gene encoding the FdsA subunit, to yield pTrc12HLB-FdsGBCD. The pTrc12HLB-FdsGBCD plasmid was transformed into *E. coli* DH5α cells, and the protein FdsBG was expressed using the same procedure as described above. In addition, the plasmid pTrc12HLB-FdsGBCD was further modified by replacing the His_6-linker-His_6 tag with a Twin-Strep® tag (IBA, Gottingen, Germany; Twin-Strep tag sequence: WSHPQFEKGGGSGGGSGGSAWSHPQFEKSG) to yield pTrc-strep-FdsGBCD. The construction of this plasmid was outsourced (Epoch Life Science, Sugar Land, TX).

For overexpression of the FdsBG complex, the pTrc-strep-FdsGBCD plasmid was transformed into *E. coli* DH5α cells. A 50-ml starter culture of Luria broth medium supplemented with 100 μg/ml ampicillin was grown overnight at 37 °C. The overnight culture was used to inoculate two 6-liter Erlenmeyer flasks, each containing 2 liters of TB medium supplemented with 100 μg/ml ampicillin and grown at 30 °C and 200 rpm to an OD_{600} of ~0.4, at which time they were induced with 0.25 mM isopropyl 1-thio-β-D-galactopyranoside. The induced cells were grown for an additional 16 h at 30 °C and 160 rpm (final OD_{600} ~12–16). Harvested cells were frozen in liquid nitrogen and stored at −80 °C until further use.

Purification of His_6-linker-His_6–tagged FdsBG complex—All steps were performed on ice or at 4 °C. Frozen cells were thawed and suspended in 40 mM KPO_4, 10 mM KNO_3, pH 7.2, in the presence of lysozyme, DNase I, 0.5 mM PMSF, 1 mM benzamidine HCl, and 1 mM NaF. The resuspended cells were passed 1–2 times through a French Press at 10,000–15,000 p.s.i. Cell debris was removed by centrifugation for 45 min at 200,000 × *g*.

For the initial purification, a 20–40% $(NH_4)_2SO_4$ cut was performed. The collected $(NH_4)_2SO_4$ cut was dissolved in 40 mM KPO_4, 10 mM KNO_3, pH 7.5, containing 15 mM imidazole, 0.5 mM PMSF, 1 mM benzamidine HCl, and 1 mM NaF. The supernatant was incubated for 1 h with nickel-nitrilotriacetic acid–agarose beads (Qiagen, Germantown, MD). The beads

were then transferred into an empty column and washed with five column volumes of resuspension buffer containing 45 mM imidazole. The FdsABG holoenzyme and FdsBG complex were eluted from the column with 300 mM imidazole. Ammonium sulfate was added to the eluent to 50% saturation, and the precipitate was collected. To reduce the contact time (~1.5 h) between FdsBG complex and the nickel-nitrilotriacetic acid resin, the chromatography was performed with a head pressure of ~2 p.s.i. of N_2.

The ammonium sulfate precipitate was treated in one of two ways. For preparations containing only FdsBG complex (the product of the overexpression of pTrc12HLB-FdsGBCD plasmid), no further purification was performed. The precipitate was resuspended and buffer-exchanged into 10 mM HEPES-NaOH, pH 7.2, with a PD-10 column (GE Healthcare) or by ultrafiltration with an Amicon Ultra with an molecular weight cuf-off (MWCO) of 50,000 (MilliporeSigma, Burlington, MA).

For preparations containing a mixture of FdsABG holoenzyme and FdsBG complex (the product of the overexpression from pTrc12HLB-FdsGBACD plasmid), the ammonium sulfate precipitate was dissolved in resuspension buffer containing 150 mM NaCl. The FdsBG complex was separated from FdsABG holoenzyme by gel filtration (Superdex 200 PG, GE Healthcare). The concentration and quality of FdsBG complex for each fraction of the gel filtration chromatography were assessed by the ratio of the absorption at 280 and 450 nm; pure FdsBG complex has a 280/450 nm ratio of 3.4. Fractions of sufficient purity and quality were combined, concentrated by ultrafiltration, and buffer-exchanged into 10 mM HEPES-NaOH, pH 7.2, with a PD-10 column or by ultrafiltration with an Amicon Ultra with an MWCO of 50,000. The concentrated protein from both preparations was aliquoted, flash-frozen in liquid nitrogen, and stored in liquid nitrogen until further use.

Purification of Twin-Strep–tagged FdsBG complex—All steps were performed on ice or at 4 °C. Frozen cells were thawed and resuspended in 40 mM KPO_4, pH 7.5, in the presence of lysozyme, DNase I, 0.5 mM PMSF, 1 mM benzamidine HCl, and 1 mM NaF. The resuspended cells were passed 1–2 times through a French Press at 10,000–15,000 p.s.i. Cell debris was removed by centrifugation, and the clarified supernatant was loaded onto a 10-ml Strep-Tactin® XT Superflow® column (IBA, Gottingen, Germany) with a 2.5-cm diameter at 0.5 ml/min. The flow-through was loaded an additional time over the Strep-Tactin® column before washing the column with 40 column volumes of resuspension buffer. FdsBG complex was eluted with resuspension buffer containing 50 mM biotin. The eluent was concentrated by ultrafiltration and buffer-exchanged into 10 mM HEPES-NaOH, pH 7.2, with a PD-10 column or by ultrafiltration using an Amicon Ultra with an MWCO of 50,000. The protein was aliquoted, flash-frozen in liquid nitrogen, and stored in liquid nitrogen until further use.

Structure determination of the FdsBG complex by X-ray crystallography

Crystallization—His_6-linker-His_6–tagged FdsBG complex was crystallized under anaerobic conditions by vapor diffusion in a sitting-drop format. 3 μl of FdsBG complex at 2.5 mg/ml were mixed with 1 μl of reservoir solution and set up over 500 μl of reservoir solution. Oxygen was removed from all solutions used for crystallization by bubbling ISP-grade nitrogen through them. 5 mM DTT was added to the FdsBG stock solution prior to the removal of the oxygen. Crystals for native and anomalous data collection were grown over 5–6.5% (v/v) isopropyl alcohol, 0–1.25% (v/v) *n*-propanol, 1.6 M $(NH_4)_2SO_4$, pH 7.5, at 16–18 °C and appeared within 2 days. Twin-Strep–tagged FdsBG complex was crystallized over 2–3% (v/v) isopropyl alcohol, 1.4 M $(NH_4)_2SO_4$, pH 7.5, at 14 °C and appeared within 3 days.

Crystals were stabilized by the successive addition of reservoir solution containing no isopropyl alcohol but increasing concentrations of glycerol to a final concentration of 24% (v/v). The thus stabilized crystals were mounted and flash-frozen in liquid nitrogen. For NADH-bound FdsBG complex, stabilized Twin-Strep–tagged FdsBG crystals were soaked for an additional 45 min in final stabilization solution containing 10 mM NADH, before mounting and flash-freezing in liquid nitrogen.

Data collection—X-ray diffraction data of native FdsBG crystals were collected at the Se-absorption edge (0.97–1.00 Å) on the 5.0.1 and 5.0.2 beamlines at the Advanced Light Source (ALS) at Lawrence Berkeley National Laboratory (LBNL) and on the 24 ID-C and 24 ID-E beamlines at the Advanced Photon Source (APS) at Argonne National Laboratory (ANL). Anomalous X-ray diffraction data were collected at the Fe absorption peak wavelength of the intrinsic iron-sulfur clusters at 1.7388 Å on the 5.0.2 beamline at ALS at LBNL, on the 24 ID-C beamline at APS at ANL, and on the BL7-1 beamline at the Stanford Synchrotron Radiation Lightsource (SSRL) at the SLAC National Accelerator Laboratory. Collected data were processed with HKL-3000 (37), DIALS (38), XDS (39), and Mosflm (40).

Structure determination—The structure was solved to a resolution of ~3.5 Å by single anomalous diffraction–molecular replacement using the Crank2-SAD/MR pipeline (41) as implemented in CCP4 (42). The search model for molecular replacement was generated based on the homology of FdsB and FdsG to Nqo1 and Nqo2 from NADH dehydrogenase of *T. thermophilus* (chain 1 and 2 in the 2FUG PDB file (11)) using the SWISS-MODEL web server (43). To improve the completeness of our high-resolution data set, two native data sets of equivalent diffraction limit were combined using the "blend" program as implemented in CCP4. The initial phases generated by single anomalous diffraction–molecular replacement were extended and refined to 2.3 Å of our high-resolution native FdsBG data set using AutoBuild and Refine as implemented in the PHENIX program suite (44, 45).

The solution of the X-ray structure shows two molecules of FdsBG complex in the asymmetric unit, which are related by an improper noncrystallographic rotation axis of ~179°. This improper rotation axis is nearly perpendicular (~92°) to the crystallographic 2-fold axis (Fig. 2*A*).

The model of the FdsBG complex was built into the high-resolution phased electron density with COOT (46) and refined with the PHENIX Refine subroutine (44). The restraints for the FMN and the Fe_2S_2 cluster were generated with eLBOW as implemented in the PHENIX program suite. The restraints file for the noncubane Fe_4S_4 cluster was taken from the GeoStd

restraints file library (https://sourceforge.net/projects/geostd/ (47)).[5] The distance and angle restraints for the covalent bonds between the iron-sulfur clusters and the cysteine residues of their binding sites in the FdsBG complex were derived from high-resolution structures of well-characterized iron-sulfur complexes. Iterative cycles of building and refining were performed until *R*-factor values converged to an R_{work} of 18.2% and R_{free} of 22.3% (see Table S1 for detailed data and refinement statistics).

The data set of the NADH-soaked crystal was solved by molecular replacement using the above solved FdsBG structure as a starting model. Iterative cycles of building and refining were performed until *R*-factor values converged to an R_{work} of 15.9% and R_{free} of 19.9% (see Table S1 for detailed data and refinement statistics).

Structure alignments were performed using secondary structure matching as incorporated in COOT, and all molecular structure figures were prepared with PyMOL (version 1.7.4, Schrödinger LLC).

Inductively coupled plasma-optical emission spectrometry (ICP-OES)

ICP-OES (Optima 7300DV (PerkinElmer Life Sciences) at the Environmental Sciences Research Laboratory, University of California, Riverside) was used to identify the metal ions present in a sample of FdsBG. Approximately 220 μl of 240 μM FdsBG complex was buffer-exchanged into 5 mM triethanolamine, pH 7.7, and then diluted with nitric acid to 65% (v/v). The sample was boiled for 10 min and then diluted to 15 ml for analysis (final nitric acid concentration ~2–3%).

EPR spectroscopy

EPR spectra were recorded using a Bruker EMX spectrometer equipped with a Bruker ER 4119HS high-sensitivity X-band cavity and gaussmeter, operated with WinEPR version 4.33 acquisition software. Temperature was controlled using a Bruker variable temperature unit and liquid nitrogen or liquid helium cryostat. For purposes of comparison, all spectra were adjusted to a microwave frequency of 9.3871 GHz. Detailed instrument settings are included in the figure legends.

Samples were made anaerobic at 4 °C and transferred to argon-flushed, septum-sealed EPR tubes. Samples prepared in this way were subsequently frozen in an ethanol/dry ice bath and transferred to liquid nitrogen. Further details of sample preparation are included in the figure legends. Simulations were performed using the EasySpin 4.5.5 software package (48). Prior to simulation of the composite spectrum described in Fig. 1*A*, parameters for the Fe/S_5 signal were estimated by graphically subtracting the spectrum of Fe/S_1. During simulations, *g*-values for the Fe/S_5 were not allowed to vary by more than 0.005, whereas anisotropic line broadening (simulated as HStrain in the EasySpin software package) varied by no more than 20 MHz. Every multicomponent simulation also included a "weight" term, which could be used to estimate the relative contribution of each component to the composite spectrum.

[5] Please note that the JBC is not responsible for the long-term archiving and maintenance of this site or any other third party hosted site.

Rapid freeze-quench EPR experiments were carried out using an apparatus described previously (49) except that the sample was not quenched by an isopentane bath at −140 °C. Instead, the reaction mixture was sprayed unto rotating silver-plated wheels immersed and equilibrated in liquid nitrogen (−196 °C) and driven by a DC motor. The large surface area of the wheels served to efficiently freeze and simultaneously grind the reaction mixture for subsequent packing into an EPR tube. The quenching time of the experiment was determined as described by Ballou and Palmer (50), taking advantage of the well-characterized pseudo-first-order kinetics of the reaction of equine metmyoglobin with azide, the $Mb{\cdot}N_3$ complex being readily detected by EPR. Double-integration of the EPR signal yields the total spin density for the $Mb{\cdot}N_3$ complex, which is then correlated with the expected kinetics. Under our experimental conditions, the quenching time was estimated to be ~40 ms.

UV-visible absorbance measurements

Activity measurements and absorbance spectra were performed using a Hewlett-Packard 8452A diode array spectrophotometer equipped with a temperature-controlled cell holder. Reductive titrations were performed with 20 mM buffered sodium dithionite and 50 μM enzyme in 100 mM KPO_4, pH 7.0, at room temperature using a custom fabricated anaerobic cuvette with sidearms (51). The level of flavin saturation was determined as described previously, by treatment of protein with 5% TCA and quantification of released flavin at 446 nm using $\epsilon = 11{,}100\ M^{-1}\ cm^{-1}$ for acidified FMN (52).

Rapid-reaction kinetics

The reaction of oxidized FdsBG complex with NADH was followed using a SX-20 stopped flow spectrophotometer (Applied Photophysics Ltd., Leatherhead, Surrey, UK) equipped with a photodiode array and a photomultiplier tube detection and operated with ProData SX 2.2.5.6 acquisition software. Time courses for the reaction were monitored at 450 nm at 5 °C and fitted to a single-exponential equation by nonlinear least squares regression analysis using the software ProData Viewer 4.2.0 (Applied Photophysics Ltd., Leatherhead, Surrey, UK).

Only the first 15–120 ms of each time course was analyzed. The observed rate constants, k_{obs}, were plotted against substrate concentrations to obtain the limiting rate constant for reduction, k_{red}, and the dissociation constant, K_d, using the following equation.

$$k_{obs} = k_{red}[S]/(K_d + [S]) \quad \text{(Eq. 1)}$$

For analysis of the second-order disproportionation reaction (the slow phase of the reaction of the enzyme with NADH), a 60-s trace collected at 450 nm was used to first estimate the end point of the reaction. A background value was then subtracted to bring the beginning of the second-order process to zero. The trace was then subtracted from the end point value, and a $\Delta\epsilon = 7200\ M^{-1}\ cm^{-1}$ was estimated empirically, assuming all 5 μM of NADH were converted to the neutral semiquinone at the end of the fast phase and that disproportion proceeded to completion

by the end of the slow phase. The data were then converted to molar concentrations using the $\Delta\epsilon$ calculated above, and time *versus* reciprocal concentrations was plotted. The second-order rate constant was calculated by linear regression analysis of the data in the 2–5-s range.

Data availability

All atomic coordinates and structure factors can be found in the Research Collaboratory for Structural Bioinformatics Protein Data Bank under accession numbers 6VW8 for the FdsBG complex and 6VW7 for the NADH-bound FdsBG complex. All data are included in the article.

Author contributions—T. Y., D. N., S. H., R. H., and G. M. B. conceptualization; T. Y., D. N., S. H., T. K. T., X. Y., R. H., and G. M. B. resources; T. Y., D. N., S. H., T. K. T., X. Y., R. H., and G. M. B. data curation; T. Y., D. N., R. H., and G. M. B. validation; T. Y., D. N., and G. M. B. visualization; T. Y., D. N., R. H., and G. M. B. writing-original draft; T. Y., D. N., S. H., T. K. T., R. H., and G. M. B. writing-review and editing; D. N., R. H., and G. M. B. formal analysis; D. N., S. H., T. K. T., R. H., and G. M. B. investigation; D. N., S. H., R. H., and G. M. B. methodology; R. H. and G. M. B. software; R. H. and G. M. B. supervision; R. H. and G. M. B. funding acquisition; R. H. and G. M. B. project administration.

Acknowledgments—We thank Tim Rowsell for critical reading of the manuscript. In addition, we thank the staff of beamlines 5.0.1 and 5.0.2 of the Berkeley Center of Structural Biology at Advanced Light Source (ALS), of beamline 24-ID-C of the Northeastern Collaborative Access Team at Advanced Photon Source (APS), and of beamline BL7-1 of the Stanford Synchrotron Radiation Lightsource (SSRL) for their support and expertise during data collection. We also thank David H. Lyons (Department of Environmental Sciences, University of California, Riverside) for performing the ICP-OES.

References

1. Pohlmann, A., Fricke, W. F., Reinecke, F., Kusian, B., Liesegang, H., Cramm, R., Eitinger, T., Ewering, C., Pötter, M., Schwartz, E., Strittmatter, A., Voss, I., Gottschalk, G., Steinbüchel, A., Friedrich, B., and Bowien, B. (2006) Genome sequence of the bioplastic-producing "Knallgas" bacterium *Ralstonia eutropha* H16. *Nat. Biotechnol.* **24,** 1257–1262 CrossRef Medline
2. Little, G. T., Ehsaan, M., Arenas-López, C., Jawed, K., Winzer, K., Kovacs, K., and Minton, N. P. (2019) Complete genome sequence of *Cupriavidus necator* H16 (DSM 428). *Microbiol. Resour. Announc.* **8,** e00814-19 Medline
3. Friedebold, J., and Bowien, B. (1993) Physiological and biochemical characterization of the soluble formate dehydrogenase, a molybdoenzyme from *Alcaligenes eutrophus*. *J. Bacteriol.* **175,** 4719–4728 CrossRef Medline
4. Friedebold, J., Mayer, F., Bill, E., Trautwein, A. X., and Bowien, B. (1995) Structural and immunological studies on the soluble formate dehydrogenase from *Alcaligenes eutrophus*. *Biol. Chem. Hoppe Seyler* **376,** 561–568 CrossRef Medline
5. Oh, J. I., and Bowien, B. (1998) Structural analysis of the fds operon encoding the NAD^+-linked formate dehydrogenase of *Ralstonia eutropha*. *J. Biol. Chem.* **273,** 26349–26360 CrossRef Medline
6. Niks, D., Duvvuru, J., Escalona, M., and Hille, R. (2016) Spectroscopic and kinetic properties of the molybdenum-containing, NAD^+-dependent formate dehydrogenase from *Ralstonia eutropha*. *J. Biol. Chem.* **291,** 1162–1174 CrossRef Medline
7. Yu, X., Niks, D., Mulchandani, A., and Hille, R. (2017) Efficient reduction of CO2 by the molybdenum-containing formate dehydrogenase from *Cupriavidus necator* (*Ralstonia eutropha*). *J. Biol. Chem.* **292,** 16872–16879 CrossRef Medline
8. Friedrich, T., and Weiss, H. (1997) Modular evolution of the respiratory NADH:ubiquinone oxidoreductase and the origin of its modules. *J. Theor. Biol.* **187,** 529–540 CrossRef Medline
9. Hille, R., Hall, J., and Basu, P. (2014) The mononuclear molybdenum enzymes. *Chem. Rev.* **114,** 3963–4038 CrossRef Medline
10. Hille, R. (1996) The mononuclear molybdenum enzymes. *Chem. Rev.* **96,** 2757–2816 CrossRef Medline
11. Sazanov, L. A., and Hinchliffe, P. (2006) Structure of the hydrophilic domain of respiratory complex I from *Thermus thermophilus*. *Science* **311,** 1430–1436 CrossRef Medline
12. Efremov, R. G., Baradaran, R., and Sazanov, L. A. (2010) The architecture of respiratory complex I. *Nature* **465,** 441–445 CrossRef Medline
13. Boyington, J. C., Gladyshev, V. N., Khangulov, S. V., Stadtman, T. C., and Sun, P. D. (1997) Crystal structure of formate dehydrogenase H: catalysis involving Mo, molybdopterin, selenocysteine, and an Fe4S4 cluster. *Science* **275,** 1305–1308 CrossRef Medline
14. Shomura, Y., Taketa, M., Nakashima, H., Tai, H., Nakagawa, H., Ikeda, Y., Ishii, M., Igarashi, Y., Nishihara, H., Yoon, K. S., Ogo, S., Hirota, S., and Higuchi, Y. (2017) Structural basis of the redox switches in the NAD^+-reducing soluble [NiFe]-hydrogenase. *Science* **357,** 928–932 CrossRef Medline
15. Yano, T., Sled', V. D., Ohnishi, T., and Yagi, T. (1996) Expression and characterization of the flavoprotein subcomplex composed of 50-kDa (NQO1) and 25-kDa (NQO2) subunits of the proton-translocating NADH-quinone oxidoreductase of *Paracoccus denitrificans*. *J. Biol. Chem.* **271,** 5907–5913 CrossRef Medline
16. Yu, X., Niks, D., Ge, X., Liu, H., Hille, R., and Mulchandani, A. (2019) Synthesis of formate from CO_2 gas catalyzed by an O_2-tolerant NAD-dependent formate dehydrogenase and glucose dehydrogenase. *Biochemistry* **58,** 1861–1868 CrossRef Medline
17. Hartmann, T., and Leimkühler, S. (2013) The oxygen-tolerant and NAD^+-dependent formate dehydrogenase from *Rhodobacter capsulatus* is able to catalyze the reduction of CO_2 to formate. *FEBS J.* **280,** 6083–6096 CrossRef Medline
18. Ohnishi, T., Ohnishi, S. T., and Salerno, J. C. (2018) Five decades of research on mitochondrial NADH-quinone oxidoreductase (complex I). *Biol. Chem.* **399,** 1249–1264 CrossRef Medline
19. Reda, T., Barker, C. D., and Hirst, J. (2008) Reduction of the iron-sulfur clusters in mitochondrial NADH:ubiquinone oxidoreductase (complex I) by EuII-DTPA, a very low potential reductant. *Biochemistry* **47,** 8885–8893 CrossRef Medline
20. Schulte, M., Frick, K., Gnandt, E., Jurkovic, S., Burschel, S., Labatzke, R., Aierstock, K., Fiegen, D., Wohlwend, D., Gerhardt, S., Einsle, O., and Friedrich, T. (2019) A mechanism to prevent production of reactive oxygen species by *Escherichia coli* respiratory complex I. *Nat. Commun.* **10,** 2551 CrossRef Medline
21. Marchler-Bauer, A., Bo, Y., Han, L., He, J., Lanczycki, C. J., Lu, S., Chitsaz, F., Derbyshire, M. K., Geer, R. C., Gonzales, N. R., Gwadz, M., Hurwitz, D. I., Lu, F., Marchler, G. H., Song, J. S., *et al.* (2017) CDD/SPARCLE: functional classification of proteins via subfamily domain architectures. *Nucleic Acids Res.* **45,** D200–D203 CrossRef Medline
22. Hinchliffe, P., and Sazanov, L. A. (2005) Organization of iron-sulfur clusters in respiratory complex I. *Science* **309,** 771–774 CrossRef Medline
23. Wallace, A. C., Laskowski, R. A., and Thornton, J. M. (1995) LIGPLOT: a program to generate schematic diagrams of protein-ligand interactions. *Protein Eng.* **8,** 127–134 CrossRef Medline
24. Olson, J. S., Ballou, D. P., Palmer, G., and Massey, V. (1974) The mechanism of action of xanthine oxidase. *J. Biol. Chem.* **249,** 4363–4382 Medline
25. Chánique, A. M., and Parra, L. P. (2018) Protein engineering for nicotinamide coenzyme specificity in oxidoreductases: attempts and challenges. *Front. Microbiol.* **9,** 194 CrossRef Medline
26. Edmondson, D. E., and Tollin, G. (1983) Semiquinone formation in flavo- and metalloflavoproteins. *Top. Curr. Chem.* **108,** 109–138 CrossRef Medline
27. Edmondson, D. E., Ackrell, B. A., and Kearney, E. B. (1981) Identification of neutral and anionic 8 α-substituted flavin semiquinones in flavopro-

teins by electron spin resonance spectroscopy. *Arch. Biochem. Biophys.* **208,** 69–74 CrossRef Medline
28. Palmer, G., Mueller, F., and Massey, V. (1971) Electron paramagnetic resonance studies on flavoprotein radicals. in *Flavins and Flavoproteins* (Kamin, H., ed) pp. 132–140, University Park Press, Baltimore
29. Cramm, R. (2009) Genomic view of energy metabolism in *Ralstonia eutropha* H16. *J. Mol. Microbiol. Biotechnol.* **16,** 38–52 CrossRef Medline
30. Bliven, S., Lafita, A., Parker, A., Capitani, G., and Duarte, J. M. (2018) Automated evaluation of quaternary structures from protein crystals. *PLoS Comput. Biol.* **14,** e1006104 CrossRef Medline
31. Krissinel, E., and Henrick, K. (2007) Inference of macromolecular assemblies from crystalline state. *J. Mol. Biol.* **372,** 774–797 CrossRef Medline
32. Runswick, M. J., Fearnley, I. M., Skehel, J. M., and Walker, J. E. (1991) Presence of an acyl carrier protein in NADH:ubiquinone oxidoreductase from bovine heart mitochondria. *FEBS Lett.* **286,** 121–124 CrossRef Medline
33. Sackmann, U., Zensen, R., Röhlen, D., Jahnke, U., and Weiss, H. (1991) The acyl-carrier protein in *Neurospora crassa* mitochondria is a subunit of NADH:ubiquinone reductase (complex I). *Eur. J. Biochem.* **200,** 463–469 CrossRef Medline
34. Galante, Y. M., and Hatefi, Y. (1979) Purification and molecular and enzymic properties of mitochondrial NADH dehydrogenase. *Arch. Biochem. Biophys.* **192,** 559–568 CrossRef Medline
35. Lauterbach, L., Idris, Z., Vincent, K. A., and Lenz, O. (2011) Catalytic properties of the isolated diaphorase fragment of the NAD-reducing [NiFe]-hydrogenase from *Ralstonia eutropha*. *PLoS ONE* **6,** e25939 CrossRef Medline
36. Kudin, A. P., Bimpong-Buta, N. Y., Vielhaber, S., Elger, C. E., and Kunz, W. S. (2004) Characterization of superoxide-producing sites in isolated brain mitochondria. *J. Biol. Chem.* **279,** 4127–4135 CrossRef Medline
37. Otwinowski, Z., and Minor, W. (1997) Processing of X-ray diffraction data collected in oscillation mode. *Methods Enzymol.* **276,** 307–326 CrossRef Medline
38. Winter, G., Waterman, D. G., Parkhurst, J. M., Brewster, A. S., Gildea, R. J., Gerstel, M., Fuentes-Montero, L., Vollmar, M., Michels-Clark, T., Young, I. D., Sauter, N. K., and Evans, G. (2018) DIALS: implementation and evaluation of a new integration package. *Acta Crystallogr. D Struct. Biol.* **74,** 85–97 CrossRef Medline
39. Kabsch, W. (2010) XDS. *Acta Crystallogr. D Biol. Crystallogr.* **66,** 125–132 CrossRef Medline
40. Leslie, A. G. W., and Powell, H. R. (2007) Processing diffraction data with MOSFLM. in *Nato Sci. Ser. II Math.* (Read, R. J., and Sussman, J. L., eds) pp. 41–51, Springer, Dordrecht, The Netherlands
41. Skubák, P., and Pannu, N. S. (2013) Automatic protein structure solution from weak X-ray data. *Nat. Commun.* **4,** 2777 CrossRef Medline
42. Winn, M. D., Ballard, C. C., Cowtan, K. D., Dodson, E. J., Emsley, P., Evans, P. R., Keegan, R. M., Krissinel, E. B., Leslie, A. G., McCoy, A., McNicholas, S. J., Murshudov, G. N., Pannu, N. S., Potterton, E. A., Powell, H. R., *et al.* (2011) Overview of the CCP4 suite and current developments. *Acta Crystallogr. D Biol. Crystallogr.* **67,** 235–242 CrossRef Medline
43. Waterhouse, A., Bertoni, M., Bienert, S., Studer, G., Tauriello, G., Gumienny, R., Heer, F. T., de Beer, T. A. P., Rempfer, C., Bordoli, L., Lepore, R., and Schwede, T. (2018) SWISS-MODEL: homology modelling of protein structures and complexes. *Nucleic Acids Res.* **46,** W296–W303 CrossRef Medline
44. Adams, P. D., Afonine, P. V., Bunkóczi, G., Chen, V. B., Davis, I. W., Echols, N., Headd, J. J., Hung, L. W., Kapral, G. J., Grosse-Kunstleve, R. W., McCoy, A. J., Moriarty, N. W., Oeffner, R., Read, R. J., Richardson, D. C., *et al.* (2010) PHENIX: a comprehensive Python-based system for macromolecular structure solution. *Acta Crystallogr. D Biol. Crystallogr.* **66,** 213–221 CrossRef Medline
45. Terwilliger, T. C., Grosse-Kunstleve, R. W., Afonine, P. V., Moriarty, N. W., Zwart, P. H., Hung, L. W., Read, R. J., and Adams, P. D. (2008) Iterative model building, structure refinement and density modification with the PHENIX AutoBuild wizard. *Acta Crystallogr. D Biol. Crystallogr.* **64,** 61–69 CrossRef Medline
46. Emsley, P., Lohkamp, B., Scott, W. G., and Cowtan, K. (2010) Features and development of Coot. *Acta Crystallogr. D Biol. Crystallogr.* **66,** 486–501 CrossRef Medline
47. Moriarty, N. W., and Adams, P. D. (2019) Iron-sulfur clusters have no right angles. *Acta Crystallogr. D Struct. Biol.* **75,** 16–20 CrossRef Medline
48. Stoll, S., and Schweiger, A. (2006) EasySpin, a comprehensive software package for spectral simulation and analysis in EPR. *J. Magn. Reson.* **178,** 42–55 CrossRef Medline
49. Kim, J. H., and Hille, R. (1993) Reductive half-reaction of xanthine oxidase with xanthine: observation of a spectral intermediate attributable to the molybdenum center in the reaction of enzyme with xanthine. *J. Biol. Chem.* **268,** 44–51 Medline
50. Ballou, D. P., and Palmer, G. A. (1974) Practical rapid quenching instrument for study of reaction-mechanisms by electron-paramagnetic resonance spectroscopy. *Anal. Chem.* **46,** 1248–1253 CrossRef
51. Niks, D., and Hille, R. (2018) Reductive activation of CO_2 by formate dehydrogenases. *Methods Enzymol.* **613,** 277–295 CrossRef Medline
52. Chapman, S. K., and Reid, G. A. (1999) *Flavoprotein protocols*, pp. 18 and 35–36, Humana Press, Totowa, NJ